ARTICLE

Katanin p60-like 1 sculpts the cytoskeleton in mechanosensory cilia

Landi Sun[1]*, Lihong Cui[1]*, Zhen Liu[1]*, Qixuan Wang[1], Zhaoyu Xue[1], Menghua Wu[1], Tianhui Sun[1], Decai Mao[2], Jianquan Ni[2], José Carlos Pastor-Pareja[1], and Xin Liang[1]

Mechanoreceptor cells develop a specialized cytoskeleton that plays structural and sensory roles at the site of mechanotransduction. However, little is known about how the cytoskeleton is organized and formed. Using electron tomography and live-cell imaging, we resolve the 3D structure and dynamics of the microtubule-based cytoskeleton in fly campaniform mechanosensory cilia. Investigating the formation of the cytoskeleton, we find that katanin p60-like 1 (kat-60L1), a neuronal type of microtubule-severing enzyme, serves two functions. First, it amplifies the mass of microtubules to form the dense microtubule arrays inside the sensory cilia. Second, it generates short microtubules that are required to build the nanoscopic cytoskeleton at the mechanotransduction site. Additional analyses further reveal the functional roles of Patronin and other potential factors in the local regulatory network. In all, our results characterize the specialized cytoskeleton in fly external mechanosensory cilia at near-molecular resolution and provide mechanistic insights into how it is formed.

Introduction

Mechanotransduction is a cellular process that converts external mechanical stimuli into intracellular signals (Gillespie and Walker, 2001; Lumpkin et al., 2010). It is the key mechanism underlying the perception of touch, sound, and acceleration. In mechanotransduction, external forces impinging on sensory cells are thought to be directly coupled to force-sensitive channels (Corey and Hudspeth, 1983; Gillespie and Walker, 2001), for which a mechanical pathway is thought to be formed by cellular structures, including the extracellular matrix, membrane, and cytoskeleton (Gillespie and Walker, 2001). Among these components, cytoskeletons are often found at the site of mechanotransduction; for example, F-actin bundles in the stereocilia of vertebrate hair cells (Gillespie and Müller, 2009), microtubules in the nonciliated touch receptors of *Caenorhabditis elegans* (Cueva et al., 2007), and in fly ciliated mechanoreceptors (Bechstedt et al., 2010; Keil, 1997). Because these cytoskeletons play both structural and sensory roles in mechanosensation (Cueva et al., 2007; Liang et al., 2014), how they are organized and formed is important in understanding the mechanism of cell mechanotransduction.

External mechanosensory (ES) organs, including campaniform and bristle receptors, belong to type I sensory receptors of *Drosophila melanogaster* (Keil, 1997). In ES organs, the dendrite of the sensory neuron is separated into the outer segment located at the distal tip and the inner segment at the proximal part by a short "9+0" cilium (Keil, 1997; Liang et al., 2013). The outer segment is a cilium-based entity that contains a mechanoreceptive organelle (MO) and a tubular body (TB). There is a large quantity of microtubules inside the outer segment (Bechstedt et al., 2010; Keil, 1997). These microtubules show a relatively high level of acetylation (Liang et al., 2011) and form a specialized cytoskeleton (Bechstedt et al., 2010; Keil, 1997; Liang et al., 2014), which structurally supports the sensory cilium and functionally contributes to mechanotransduction (Liang et al., 2014). However, the structural and molecular basis of this cytoskeleton remains unknown. First, the ultrastructural organization and stability of these microtubules have not been characterized. Second, how the cytoskeleton is formed remains elusive. A previous study on *dcx-emap* suggests the presence of specific regulatory proteins in the outer segment (Bechstedt et al., 2010). However, their identity and working mechanism remain unknown.

Campaniform mechanoreceptors are located at joints (e.g., wing base; Keil, 1997; Liang et al., 2017), and they respond to various types of cuticular strains caused by internal (e.g., muscular activity) or external (e.g., mechanical compression) mechanical stimuli to provide sensory feedbacks (Pringle et al., 1948). The characteristic dome-like external structures and their localizations near the cuticular surface facilitate the study of these receptors using electron and light microscopy (Liang

[1]Tsinghua-Peking Joint Center for Life Science, School of Life Sciences, Tsinghua University, Beijing, China;   [2]School of Medicine, Tsinghua University, Beijing, China.

*L. Sun, L. Cui, and Z. Liu contributed equally to this paper;   Correspondence to Xin Liang: xinliang@tsinghua.edu.cn.

et al., 2013; Sun et al., 2019a). Furthermore, the high similarity among different ES organs makes it possible to use campaniform mechanoreceptors as a model to study the sensory neuron in fly ES organs.

In the present study, we resolved the 3D structure of the cytoskeleton in the outer segment of campaniform mechanoreceptors using electron tomography (ET) and showed that this cytoskeleton is formed of mostly unidirectional and stable microtubules using light microscopy. Furthermore, we identified that katanin p60-like 1 (kat-60L1), a neuronal type of microtubule-severing enzyme, contributes to mechanosensitivity and sculpts the cytoskeleton in the mechanosensory cilia. Structural analyses on mutants suggest that kat-60L1 amplifies the mass of microtubules to form dense microtubule arrays and generates short microtubules to build the nanoscopic cytoskeleton in the MO. Further analyses reveal the functional roles of Patronin and other potential regulatory factors in promoting microtubule assembly and stability in the outer segment. In all, our results characterize the specialized cytoskeleton in fly mechanosensory ES organs in detail and provide mechanistic insights into how the cytoskeleton is formed.

Results

The outer segment contains two ordered arrays of microtubules

We set out to reconstruct the outer segment of campaniform mechanoreceptors using a recently developed protocol based on ET (Sun et al., 2019a). Two types of campaniform mechanoreceptors were analyzed: the arrayed receptors in the pedicel of halteres (Fig. 1, A–I) and the isolated receptors in legs (Fig. 2, A–F; and Fig. S1). Despite the differences in detailed geometry, the outer segment in both types of cells was separated from the inner segment by a short cilium, and it contained an MO and a TB (Fig. 1, B and I; and Fig. 2, B and D). To better understand the cytoskeletal structure, we traced the microtubules in the outer segment and built the 3D model (Fig. 1 I, Fig. 2 D, and Video 1).

In haltere pedicellar receptors, the TB had a nearly spherical morphology (x axis, 1.4 ± 0.7 μm; y axis, 1.4 ± 0.7 μm; z axis, 1.2 ± 0.6 μm; n = 3 receptors). Nine microtubule doublets were curved to fit the dilated shape of the TB and embraced an array of interconnected microtubules inside the TB (Fig. 1 I). By inspecting the positions of microtubule ends that appeared within the volume of tomographic reconstruction (Fig. S2), we found that microtubules in the TB were short (L_{TB_MT} = 296 ± 191 nm, n = 2,524 microtubules from four cells). They were mostly aligned to the proximal–distal axis, but some transversely oriented ones were also observed in the peripheral region. The distal end of the TB formed a neck-like region in transition to the MO (Fig. 1, D and I). In the MO, short microtubules (L_{MO_MT} = 221 ± 88 nm, n = 352 microtubules from four cells) were organized into two-line arrays with the electron-dense materials in between (Fig. 1 C), together forming a nanoscopic cytoskeleton. We noted that microtubules in the TB never extended into the MO (zero in four complete sets of volume data), suggesting that microtubules in the outer segment are organized into two arrays.

In leg receptors, we collected mostly lateral sections for technical reasons (see Materials and methods). The outer segment

of leg receptors showed an almond-shaped morphology (Fig. 2 C). Similar to haltere receptors, microtubules in the MO were embedded in the electron-dense materials. However, no neck-like region was found. Because lateral sections do not allow direct length measurement (Fig. S2), we measured the spatial distribution of microtubule ends in the outer segment. The distal ends of microtubules accumulated at two regions: the distal tip of the outer segment and the border region between the MO and TB (Fig. 2, E and F). The proximal ends also accumulated at two regions: the border region and the proximal end of the TB (Fig. 2, E and F). Close inspection revealed that only a small number of microtubules spanned across the MO and TB (10 in all 140 MO microtubules [7%] in five cells; Fig. 2 F), suggesting that microtubules in the MO were mostly shorter than 800 nm and were separate from those in the TB. Therefore, microtubules in the outer segments of leg receptors are also organized into two arrays, suggesting a common ultrastructural organization of microtubules in fly campaniform mechanosensory cilia.

Microtubules in the outer segment have a "plus end–distal" polarity

Having built the structural model, we wondered about the polarity of microtubules in the TB and MO. We first examined the localization of Patronin, a microtubule minus end stabilizing factor (Goodwin and Vale, 2010; Hendershott and Vale, 2014). To avoid overexpression artifact, we generated a Patronin-RFP knock-in (KI) strain (Fig. S1). In the MO of haltere receptors, Patronin signal was enriched at the proximal end (Fig. 3 A), suggesting that the short microtubules in the MO have a "plus end–distal" polarity. In the TB, Patronin showed a diffusive distribution (Fig. 3 A), consistent with most of microtubules being short and the presence of transversely oriented microtubules. To further clarify the polarity of microtubules in the TB, we studied leg receptors (Fig. S1). Patronin showed two enriched signals in the outer segment of leg receptors (Fig. 3 B). The distal signal of Patronin was 0.6 ± 0.1 μm (n = 13 receptors) away from the distal tip of the outer segment, corresponding to the border region between the MO and TB. The proximal signal of Patronin appeared at the proximal end of the TB, where many microtubule ends are located (Fig. 2 E). Therefore, we conclude that most of microtubules in the TB have a plus end–distal orientation.

We also recorded EB1 signals in the outer segment of leg receptors. EB1 comets in the outer segment showed very short trajectories (Fig. 3 C and Video 2), so we cannot measure the moving directions. Instead, we quantified the distribution of EB1 signal along the proximal-distal axis of the outer segment (Fig. 3 D). EB1 signal at the distal end was 135 ± 12% of that at the proximal end (n = 5 cells; P < 0.001; Fig. 3 E). The region with a stronger EB1 signal covered the MO and the distal part of the TB, supporting the idea that most of microtubules in the TB have a plus end–distal polarity. Furthermore, the observation of an EB1 signal at the distalmost tip (Fig. 3 C) and the enrichment of Patronin at the proximal end of the MO (Fig. 3, A and B) suggest that microtubules in the MO also have a plus end–distal orientation.

In contrast to the outer segment, all EB1 comets in the inner segment (n = 5 cells) moved toward the cell body (Video 2),
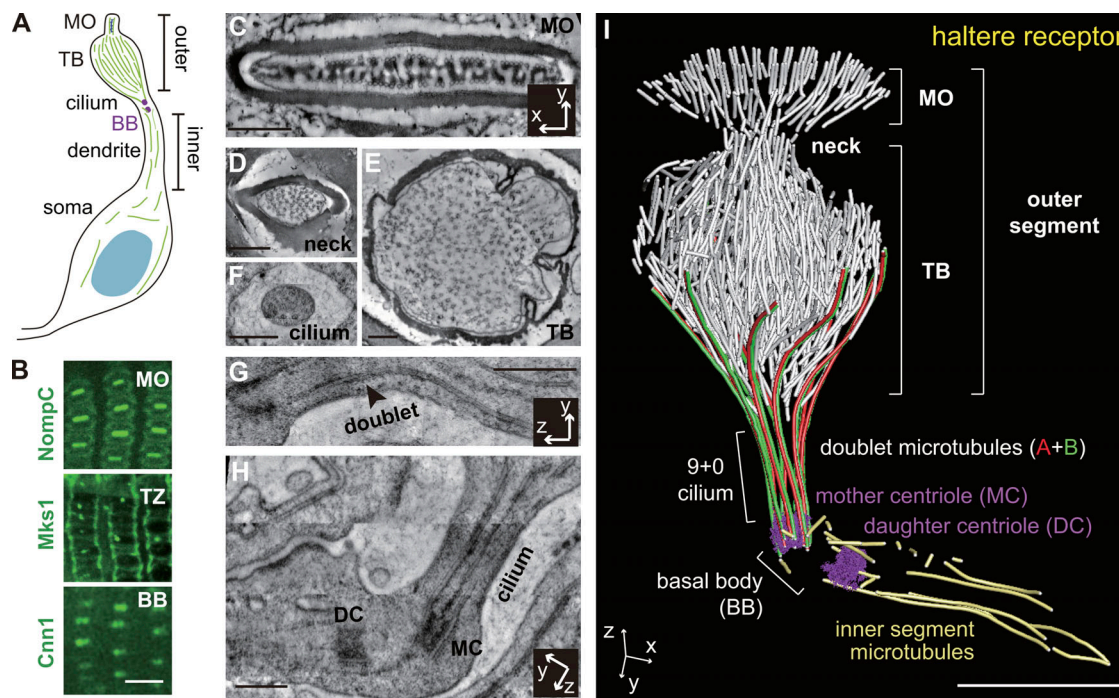
Figure 1. **Ultrastructural organization of microtubules in the outer segment of haltere campaniform receptors. (A)** Cartoon schematic of the sensory neuron in haltere receptors. BB, basal body. **(B)** The localizations of NompC-GFP (MO), Mks1-GFP (transition zone [TZ]), and GFP-Cnn1 (BB) in haltere receptors (top view). Upper: *nompC-gfp-KI*. Middle: *Mks1-gfp*. Lower: *uas-gfp-cnn1/+; +/+; dcx-emap-gal4/+*. Scale bar, 5 µm. **(C–F)** Cross-sectional views of the MO (C), neck (D), TB (E), and cilium (F). **(G)** Lateral view of the cilium. Black arrowhead, a doublet. **(H)** Lateral view of the mother centriole (MC), daughter centriole (DC), and cilium. Scale bars (C–H), 250 nm. C–H are ET slice images. **(I)** Reconstructed model of microtubules in the outer segment. Each microtubule was shown as a rod. White, microtubule in the outer segment. Red (tubule-A) and green (tubule-B), doublet. Yellow, microtubule in the inner segment. Scale bar, 1 µm. Also see Video 1.

indicating that these microtubules have a "minus end–distal" orientation. This is consistent with previous studies on the polarity of dendritic microtubules in fly neurons (Stone et al., 2008; Wang et al., 2019). We also noted two dot-shaped signals of Patronin appearing around the proximal end of the TB in both haltere and leg receptors (Fig. 3, A and B). Using live-cell imaging and ET, we found that these two dots were outside the sensory neuron and were associated with a group of microtubules in the thecogen cell that wraps the dendrite of the sensory neuron in campaniform mechanoreceptors (Fig. S1).

Microtubules in the outer segment are stable

We then measured the stability of microtubules in the outer segment using FRAP (Fig. 3 F). Leg receptors were used in this experiment due to the convenience of obtaining lateral views. We found that the tubulin signal in the inner segment fully recovered in 3 h, while that in the outer segment recovered to only ~25% (Fig. 3 G), suggesting that microtubules in the outer segment are more stable. To further justify this conclusion, two issues were considered. First, does the tubulin signal reflect the mass of microtubules or soluble tubulin dimers? We found that the density of microtubules in the outer segment was 156 ± 29 µm^{-2} (n = 5 receptors), leading to an estimation that microtubules contributed to ~98% of the fluorescence tubulin signal (Fig. S2). Similarly, the microtubule density in the inner segment was 25 ± 11 µm^{-2} (n = 3 receptors), suggesting that microtubules contributed to ~87% of the tubulin signal (Fig. S2).

Therefore, we conclude that the intensity of the tubulin signal (Fig. 3 G) reflects the mass of microtubules. Second, could the signal recovery in the outer segment be limited by the transportation of GFP-tagged tubulin dimers into the sensory cilium? As a control, the signal recovery of EB1-tandem dimer (td) GFP (dimeric, ~116 kD), which has a similar molecular weight to GFP-αtub84B/βtub dimer (~125 kD), was measured. EB1 signal in the outer segment showed a rapid recovery (τ = 2.2 ± 0.3 min, n = 6 cells; Fig. 3 G), which is an order of magnitude faster than tubulin recovery (τ = 48.1 ± 9.8 min, n = 10 cells; Fig. 3 G), suggesting that the transportation of GFP-tubulin cannot be a limiting step. Therefore, we conclude that the fluorescence recovery reflects microtubule turnover, and that the slower turnover rate in the outer segment suggests greater stability.

Based on the structure and dynamics analyses, we conclude that microtubules in the outer segment are mostly unidirectional and stable. In addition, they are organized into two arrays, i.e., a nanoscopic one in the MO and a relatively bigger one in the TB (Fig. 3 H).

Kat-60L1 contributes to mechanosensation

Having characterized the structure and dynamics of the microtubule arrays in the outer segment, we wondered how they are formed. In a previous DNA array analysis (Bechstedt, 2006; Bechstedt et al., 2010), *kat-60L1*, a katanin family member, was found to be highly expressed in fly halteres. Because microtubules in the outer segment, especially those in the MO, are
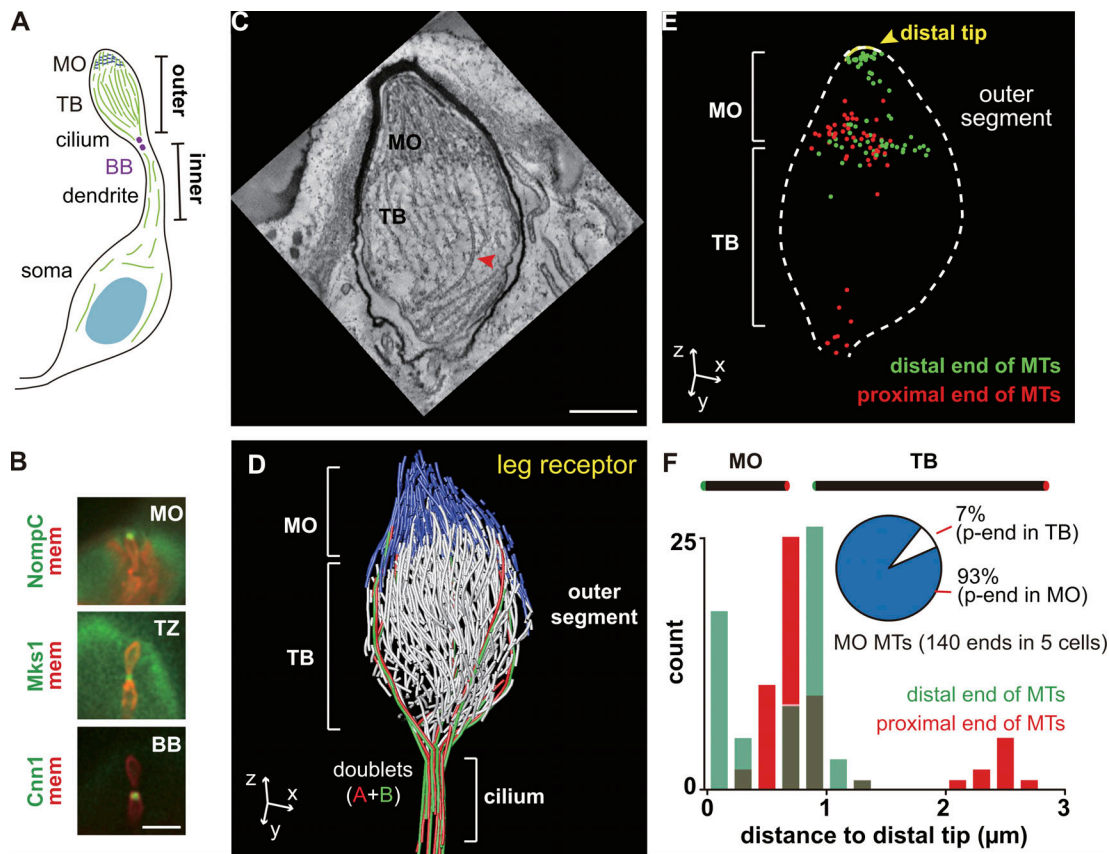
Figure 2. **Ultrastructural organization of microtubules in the outer segment of leg campaniform receptors. (A)** Cartoon schematic of the sensory neuron in leg receptors. **(B)** The localizations of NompC-GFP (MO), Mks1-GFP (transition zone [TZ]), and GFP-Cnn1 (basal body [BB]) in leg receptors (lateral view). Upper: *nompC-gfp-KI; dcx-emap-gal4, uas-cd4-tdTom/+*. Middle: *+/Mks1-gfp; +/dcx-emap-gal4, uas-cd4-tdTom*. Lower: *uas-gfp-cnn1/+; +/+; dcx-emap-gal4, uas-cd4-tdTom/+*. Scale bar, 5 µm. **(C)** Lateral view (ET slice image) of the outer segment. Red arrowhead, a TB microtubule. **(D)** Reconstructed model of microtubules in the outer segment. Blue, MO microtubule. White, TB microtubule. Red (tubule-A) + green (tubule-B), doublet. **(E)** Spatial distribution of microtubule ends in the outer segment. Every spot represented one end. Green, distal end. Red, proximal end. The yellow line (yellow arrowhead) indicates the distal tip. Scale bars (C–E), 500 nm. **(F)** The distribution of the distance between each microtubule end to the distal tip (representative of data from five cells). Red, proximal end. Green, distal end. The pie chart shows the percentage of MO microtubules that had the proximal end (p-end) in the TB. MT, microtubule; mem, membrane.

short, and katanin family members are ATPases that sever long microtubules into short ones (McNally and Roll-Mecak, 2018; McNally and Vale, 1993), we explored the functions of kat-60L1.

Using a gal4-driver strain (*kat-60L1-gal4*), we found that kat-60L1 expressed in haltere campaniform mechanoreceptors and other peripheral sensory cells, including larval dendritic arborization (da) neurons (Fig. 4, A and B). Based on the annotation in Flybase, kat-60L1 has two transcriptional isoforms. To examine their expression patterns, we generated two isoform-specific gal4-driver lines (*kat-60L1-short-gal4* and *kat-60L1-long-gal4*; Fig. 4 A). Kat-60L1-long expressed in peripheral sensory cells and central nervous systems, while kat-60L1-short only expresses in central nervous systems (Fig. S3). Using RT-PCR, we confirmed that only the long isoform can be detected in haltere RNA samples (Fig. 4 C). We then analyzed the subcellular localization of kat-60L1-long. Using a neuronal driver (*elav-gal4*) and two more specific neuronal drivers (*kat-60L1-long-gal4* and *dcx-emap-gal4*), we found that kat-60L1-long (RFP-kat-60L1-long) showed two subcellular localizations: (1) an enriched

signal at the basal body and (2) a diffusive signal in the outer segment (Fig. 4 D and Fig. S3).

To examine if kat-60L1 contributes to the sensory function of campaniform mechanoreceptors, we first performed flight tests (Bechstedt et al., 2010). Two mutant lines of *kat-60L1* were used, one null mutant (*BE6*; Stewart et al., 2012) and one *piggyBAC* insertion mutant (*c01236*; Lee et al., 2009). *BE6, c01236*, and *c01236/BE6* mutants all showed reduced flight ability, while expressing kat-60L1-long using a pan-neuronal driver (*elav-gal4*) or a more specific type I mechanoreceptor driver (*dcx-emap-gal4*) rescued the behavioral phenotype to a large extent (Fig. 4 E), suggesting that kat-60L1 contributes to fly mechanosensation. Using extracellular recording (Liang et al., 2013), we found that mechanotransduction still occurred in the haltere receptors of *kat-60L1* mutants but had a significantly reduced response (~45% reduction; Fig. 4, F and G), suggesting that kat-60L1 does not directly participate in mechanotransduction but likely contributes to the mechanosensitivity. Similar phenotypes were also observed in leg receptors by recording the force-invoked calcium response in vivo (Fig. 4, H–J). Based on these results, we
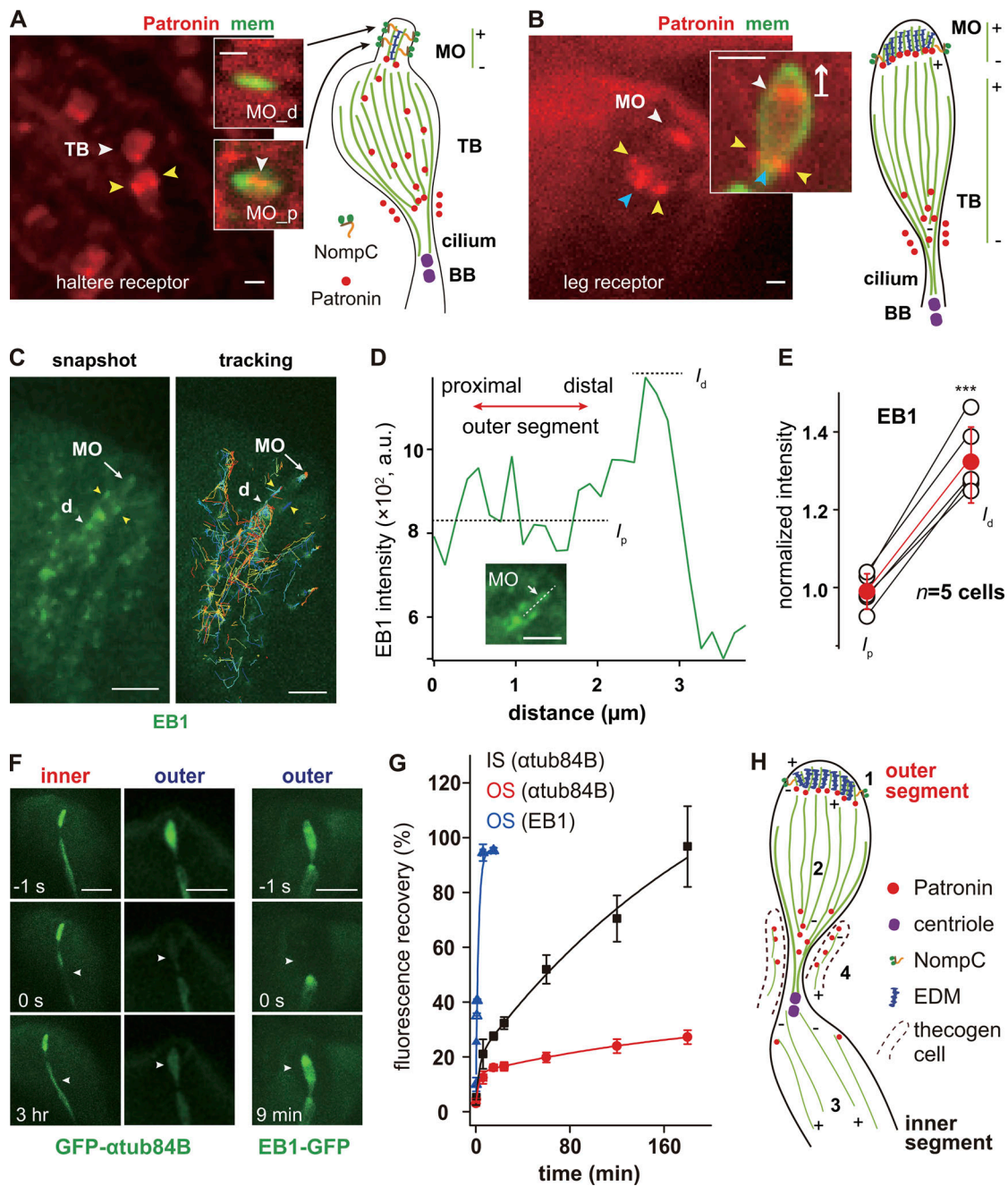
Figure 3. **Polarity and stability of microtubules in the outer segment of fly campaniform receptors. (A)** Localization of Patronin-RFP (*patronin-rfp-KI*) in haltere receptors (lateral view). White arrowhead, Patronin-RFP in the TB. Inset (top view), distal (upper) and proximal (lower) ends of the MO (*patronin-rfp-KI; dcx-emap-gal4/uas-cd4-tdgfp*). Yellow arrowhead, two dot-shaped Patronin-RFP signals outside the neuron (Fig. S1). Scale bar, 1 µm. **(B)** Localization of Patronin-RFP in leg receptors (lateral view). White arrowhead, the distal signal of Patronin-RFP (inset, 600 nm from the distal tip). Blue arrowhead, the proximal signal of Patronin-RFP. Yellow arrowheads, two dot-shaped Patronin-RFP signals outside the neuron (Fig. S1). Scale bar, 1 µm. **(C)** EB1 comets (*EB1-tdgfp-KI*) in leg receptors. Left panel: A snapshot of EB1 comets (Video 2). White arrow, MO. Yellow arrowheads, two dot signals associated with the microtubules outside the neuron. Right panel: The trajectories of EB1 comets in 3 min. White arrowhead: dendritic inner segment (d). Scale bars, 5 µm. **(D)** Intensity line profile of EB1 signal in the outer segment along the proximal–distal axis (inset). The signals at the distal end (I_d) and at the proximal part (I_p) were quantified. Scale bar (inset), 3 µm. **(E)** Statistical quantification of EB1 signal at the distal end (I_d) and the proximal end (I_p; n = 5 cells). The data were presented as mean ± SD with scattered data points. Two-sided unpaired Student's t test. ***, P < 0.001. **(F)** Three sets of representative confocal images (−1 s: right before bleaching; 0 s: just after bleaching; 3 h or 9 min: time after bleaching) showing the recovery of GFP-tubulin (*dcx-emap-gal4/uas-gfp-αtub84B*) or EB1-GFP (*dcx-emap-gal4; uas-EB1-gfp*). Scale bars, 5 µm. **(G)** Fluorescence recovery curves after photobleaching. Red (circle), GFP-tubulin recovery in the outer segment (n = 10 cells). Black (square), GFP-tubulin recovery in the inner segment (n = 9 cells). Blue (triangle), EB1-GFP recovery in the outer segment (n = 6 cells). Data were presented as mean ± SEM. **(H)** Cartoon schematic of four groups of microtubules. 1, microtubules in the MO. 2, microtubules in the TB. 3, microtubules in the inner segment. 4, microtubules in the thecogen cell. +, plus end; −, minus end; BB, basal body; EDM, electron-dense materials; IS, inner segment; OS, outer segment; mem, membrane.
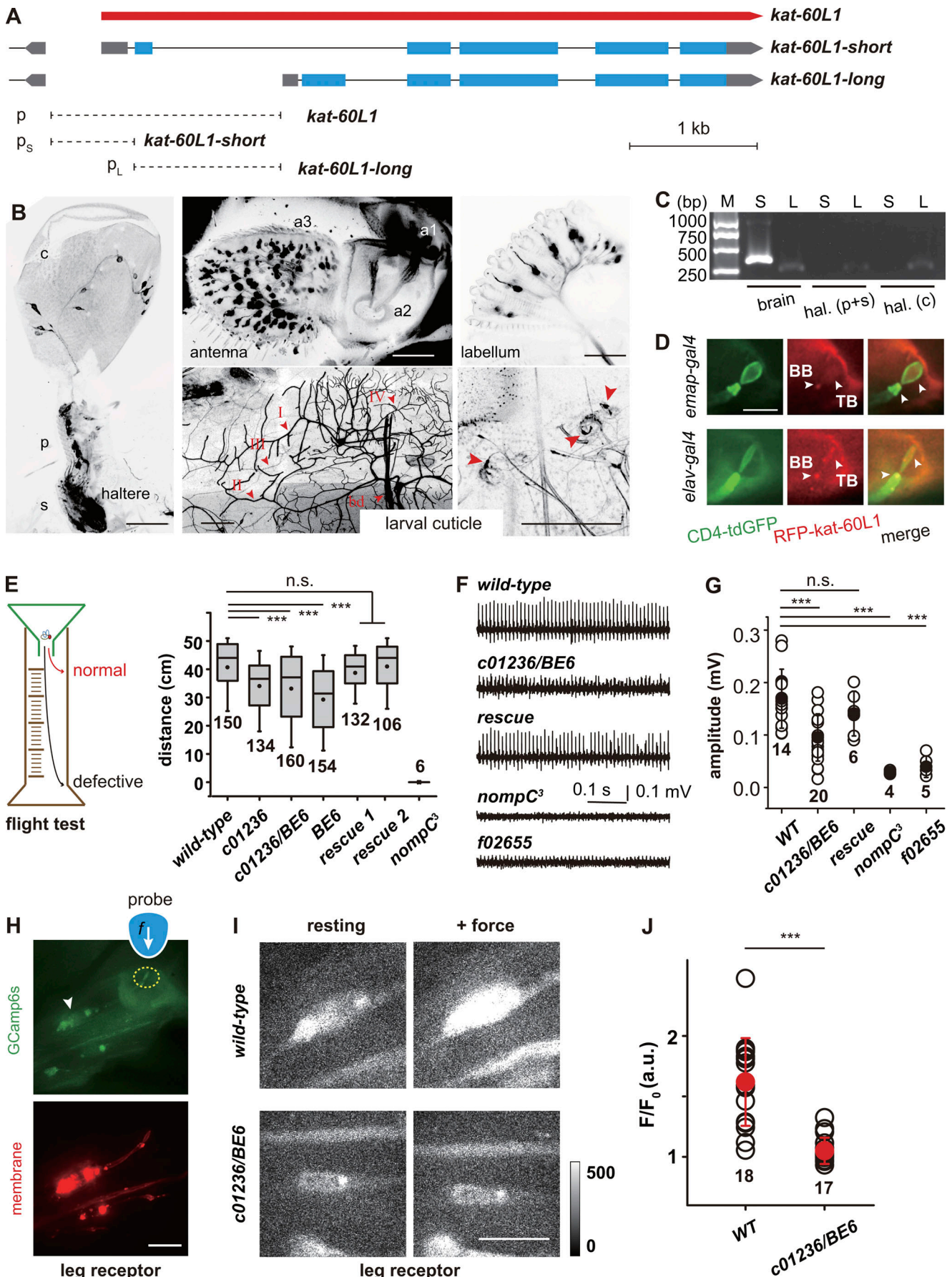
Figure 4.   Kat-60L1 contributes to mechanosensation. (A) Cartoon schematics of *kat-60L1* and its two isoforms. The promoter regions: (1) long and short isoforms (P): *kat-60L1-gal4*; (2) long isoform (P_L): *kat-60L1-long-gal4*; (3) short isoform (P_S): *kat-60L1-short-gal4*. **(B)** Kat-60L1 expressed in fly external sensory organs and larval da neurons (*kat-60L1-gal4; uas-cd4-tdgfp*). c, Capitellum; p, pedicel; s, scabellum; a, antenna segment. Arrowheads, larval da and bipolar dendrites neurons (middle bottom) and larval ES organs (right bottom). Scale bars, 50 μm. Note the representative images for different tissues were juxtaposed together for display. **(C)** A representative gel image (RT-PCR) showing that the long isoform, but not the short isoform, can be detected in haltere RNA sample, while both isoforms can be detected in brain RNA sample. M, marker; S, short isoform; L, long isoform; hal, haltere. **(D)** Localization of RFP-kat-60L1-long in leg receptors. Upper: *dcx-emap-gal4/uas-rfp-kat-60L1-long; +/uas-cd4-tdgfp*. Lower: *elav-gal4/uas-rfp-kat-60L1-long; +/uas-cd4-tdgfp*. Scale bar, 5 μm. **(E)** Flight tests on *wild type* (n = 150), *c01236* (n = 134), *c01236/BE6* (n = 160), *BE6* (n = 154), two rescue strains (1: *elav-gal4/uas-rfp-kat-60L1-long; c01236/BE6* [n = 132]; 2: *dcx-emap-gal4/uas-RFP-kat-60L1-long; c01236/BE6* [n = 106]) and *nompC³* (a negative control with abrogated mechanotransduction, n = 6). The number of flies is indicated. Two-sided unpaired Student's *t* test with Bonferroni correction. ***, P < 0.001. **(F)** Representative extracellular recording traces of *wild type*, *c01236/BE6*, the rescue strain (*elav-gal4/uas-rfp-kat-60L1-long; c01236/BE6.*), *nompC³*, and *f02655*. Note that *f02655* is a *dcx-emap* mutant with compromised cytoskeleton in the outer segment (Bechstedt et al., 2010) and is used as a negative control here. **(G)** Statistical quantification of the response amplitude in extracellular recording assays. *Wild type* (n = 14), *c01236/BE6* (n = 20), *rescue*: *elav-gal4/uas-rfp-kat-60L1-long; c01236/BE6* (n = 6), *nompC³* (n = 4), and *f02655* (n = 5). **(H)** Representative images of leg receptor in the functional assays. Upper: GCamp6s. Lower: Membrane. Yellow dashed circle, the region being compressed by the force probe. Arrowhead, soma. Scale bar, 10 μm. **(I)** Representative images of in vivo calcium recording in *wild type* (*dcx-emap-gal4, uas-cd4-tdTom/uas-GCamp6s*) and *c01236/BE6* (*dcx-emap-gal4, uas-cd4-tdTom/uas-GCamp6s; c01236/BE6*). Scale bar, 10 μm. **(J)** Statistical quantification of the calcium response amplitude. *Wild type* (n = 18), *c01236/BE6* (n = 17). In G and J, the number of flies (G) or cells (J) is indicated. Data are presented as mean ± SD with scattered data points. Two-sided unpaired Student's *t* test. ***, P < 0.001. BB, basal body; n.s., no significance.

conclude that kat-60L1-long contributes to fly mechanosensation, and its absence impairs mechanosensitivity.

The outer segment in *kat-60L1^c01236/BE6^* is disrupted

How does the loss of kat-60L1 impair mechanosensitivity? We first checked the morphology of the sensory cilium in haltere receptors. In wild-type cells, the cross-sectional view of the TB showed a ring shape with a maximum area of 3.3 ± 0.5 μm² (n = 6 halteres, 48 cells), and the MOs showed a band shape (length, 2.0 ± 0.1 μm, n = 6 halteres, 48 cells; Fig. 5, A and B). In *c01236/BE6*, the TBs had a smaller cross-sectional area (2.1 ± 0.3 μm²), and the MOs were shorter (1.4 ± 0.2 μm, n = 6 halteres, 48 cells, P < 0.001; Fig. 5, A and B). Furthermore, the signals of NompC-GFP in the MO and GFP-tubulin in the outer segment were greatly reduced in *c01236/BE6* (Fig. 5, A, C, and D). These phenotypes were confirmed at ultrastructural level using serial block-face imaging (Fig. 5, E and F; and Video 3). The outer segment in haltere receptors of *c01236/BE6* showed structural defects: the MO was shorter and wider; the neck region was less obvious; the TB contained a disrupted microtubule array and surprisingly many vesicles (Fig. 5, E and F). Based on these results, we conclude that in *c01236/BE6* mutants, the outer segment is structurally disrupted, and the levels of mechanosensory molecules, e.g., microtubule and NompC, are reduced, which could account for the impaired mechanosensitivity. We noted that the cilium of haltere receptors in *c01236/BE6* mutants lost ninefold structural symmetry, and the mother centriole showed a broken structure (Fig. 5 E). Further analyses demonstrate that these defects can be observed in haltere receptors but not in leg receptors (Fig. S4), suggesting that they are not the primary consequences of losing kat-60L1, but likely secondary effects caused by haltere-specific reasons.

Kat-60L1 is a microtubule-severing enzyme

To understand the functions of kat-60L1 at molecular level, we first examined if it could sever microtubules. Using a microtubule spin-down assay, we found that purified kat-60L1-long protein promoted microtubule disassembly in the presence of ATP (Fig. S3). In ADP condition, kat-60L1-long could bind to taxol-stabilized microtubules but lost the disassembly activity (Fig. S3). Further analyses using the total internal reflection fluorescence (TIRF)–based imaging assay showed that kat-60L1 could rapidly sever surface-bound taxol-stabilized microtubules in the presence of ATP but not ADP (Fig. S3). Therefore, kat-60L1 has an ATP-dependent microtubule-severing activity.

Kat-60L1 increases the mass of microtubules and generates short microtubules

We then analyzed microtubule arrays in the outer segment in *c01236/BE6*. ET reconstruction showed two major changes (Fig. 5, G–I; and Fig. S5). First, the total mass of microtubules in the outer segment was significantly reduced (*wild type*, 246 ± 61 μm, n = 6 cells; *c01236/BE6*, 120 ± 17 μm, n = 6 cells; P < 0.01; Fig. 5 H). Second, microtubules in the mutant outer segment were longer (Fig. 5 I). Many TB microtubules, including several doublets, extended into the MO (Fig. 5 G and Fig. S5). Therefore, the microtubule array in the MO was no longer separate from that in the TB. Consistent with this observation, Patronin signal at the proximal end of MOs was nearly absent (i.e., fewer minus ends; Fig. 5, J and K). Therefore, kat-60L1 regulates the mass and length of microtubules in the outer segment of haltere receptors.

The disrupted ciliary structure in the haltere receptors in *c01236/BE6* raises a possibility that the structural defects in the outer segment may result from the leaky ciliary gate. Therefore, to confirm our findings, we analyzed leg receptors in *c01236/BE6*, where the ciliary structures are intact (Fig. S4). The phenotypes were similar to those observed in haltere receptors. For example, the outer segment was smaller, and the signals of NompC-GFP in the MO and GFP-tubulin in the TB were reduced (Fig. 6, A–D). ET data showed that while the total mass of microtubules in the outer segment was much smaller in *c01236/BE6*, there was a significantly larger percentage of microtubules spanning across the TB and MO (Fig. 6, E–G). The absence of the distal Patronin signal further confirmed that microtubules are longer in *c01236/BE6* (Fig. 6 H). Therefore, kat-60L1 coordinates the mass and length of microtubules in the outer segment of leg receptors. We also examined if the loss of kat-60L1 leads to the same defects in other external mechanoreceptors (e.g., bristle
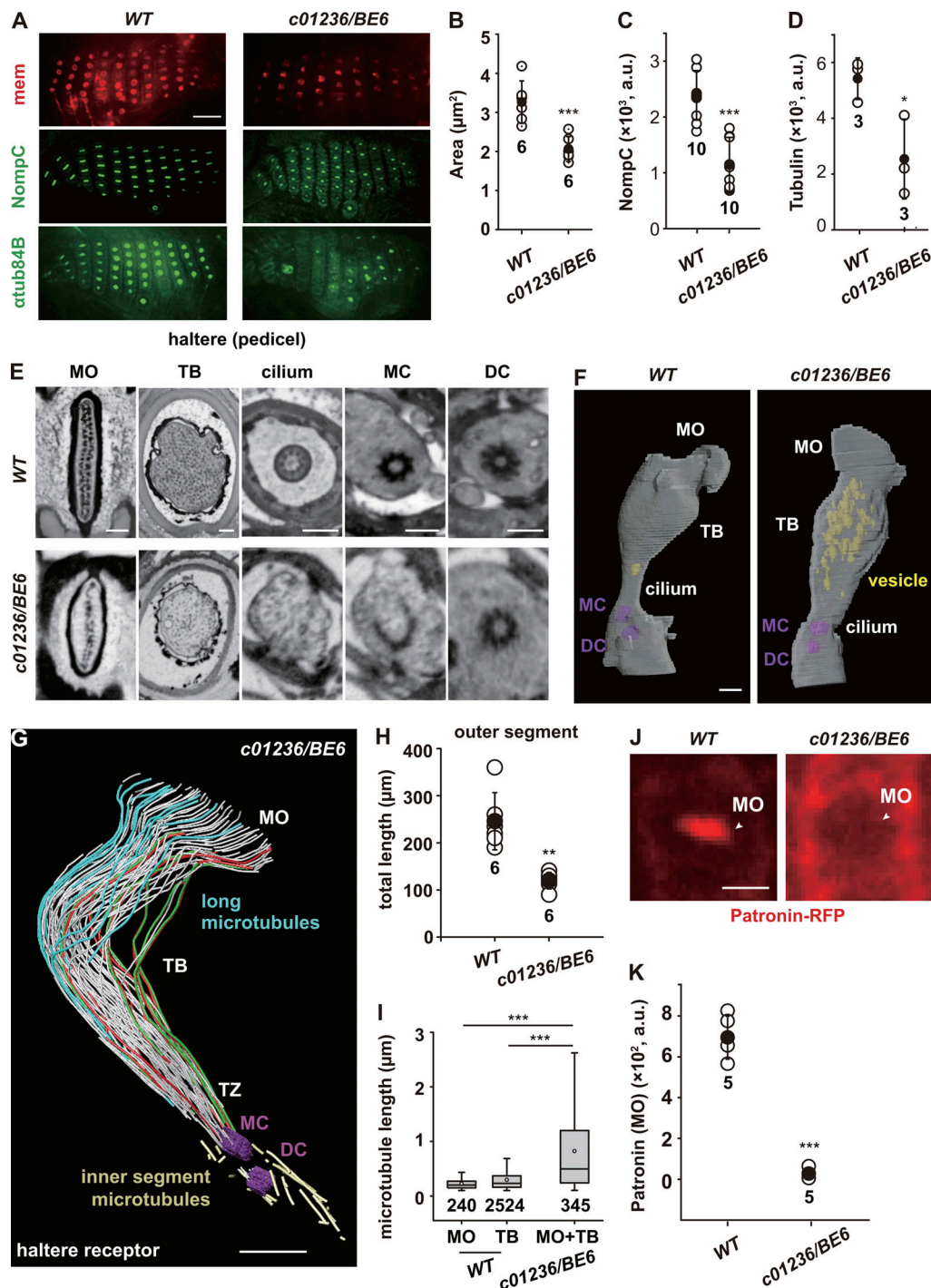
Figure 5. **Functions of kat-60L1 in haltere receptors. (A)** Representative confocal images (top view) showing the membrane, NompC, and tubulin signals in the outer segment. Upper left: *dcx-emap-gal4/uas-cd4-tdTom*. Middle left: *NompC-gfp-KI*. Lower left: *dcx-emap-gal4/uas-gfp-αtub84B*. Upper right: *dcx-emap-gal4/uas-cd4-tdTom; c01236/BE6*. Middle right: *NompC-gfp-KI; c01236/BE6*. Lower right: *dcx-emap-gal4/uas-gfp-αtub84B; c01236/BE6*. Scale bar, 10 μm. **(B)** Statistical quantification of the maximum cross-sectional area of the outer segment. **(C)** Statistical quantification of NompC-GFP signal in the MO. In B and C, the number of halteres (30 cells per haltere) is indicated. **(D)** Statistical quantification of GFP-tubulin signal in the outer segment. Note that 50% of the haltere receptors (n = 3 halteres) in *c01236/BE6* had an undetectable signal (A). The rest showed a 44% reduction (*wild type*: n = 3 halteres, 148 cells; *c01236/BE6*: n = 3 halteres, 76 cells; P < 0.05). **(E)** Representative slice images of the sensory cilium from the volume data acquired using serial block-face imaging. Upper panels: *wild type*. Lower panels: *c01236/BE6*. **(F)** Segmented model of the sensory cilium in *wild type* (left) and *c01236/BE6* (right). In E and F, scale bars, 250 nm. Also see Video 3. **(G)** Reconstructed model of microtubules in the outer segment (*c01236/BE6*). Blue, the aberrantly long microtubules. Scale bar, 0.5 μm. **(H)** Total length of microtubules in the haltere receptors of *wild-type* and *c01236/BE6* flies. The number of receptors was indicated. **(I)** The length of individual microtubules in the outer segment of haltere receptors in *wild type* and *c01236/BE6*. The data were from four and two sets of completely reconstructed wild-type and mutant volume data. The number of microtubules is indicated. Two-sided unpaired Student's *t* test with Bonferroni correction. **(J)** Representative confocal images showing Patronin-RFP signal at the proximal end of the MO in haltere receptors in *wild type* (left, *patronin-rfp-KI*) and

receptors), and similar phenotypes were observed (Fig. S5), suggesting common functions of kat-60L1 in different ES organs.

Kat-60L1 plays a destructive role in the inner segment

We noted a significantly increased tubulin signal at the distal region of the inner segment in *c01236/BE6* (Fig. 6, A and D), suggesting local accumulation of microtubules. This is confirmed by two additional observations. First, Patronin-RFP showed a more prominent signal in the inner segment in *c01236/BE6* (Fig. 6, H and I). Second, the frequency of EB1 comets in the inner segment was increased by 30% in *c01236/BE6* (Fig. 6, J and K; and Video 2), indicating more microtubule polymerization events. In all, these results demonstrate that kat-60L1 plays a destructive role in the inner segment, and in its absence, the homeostatic dynamics of microtubules in the inner segment are altered to a status that favors polymerization.

Nanoscopic cytoskeleton in the MO requires short microtubules

We showed that the loss of kat-60L1 disrupts the microtubule array in the MO, but it remains unclear whether this is simply due to overall shortage of microtubules in the outer segment or because the nanoscopic cytoskeleton in the MO requires short microtubules. To clarify this issue, we studied the knockdown mutants of *kat-60L1*. In two *kat-60L1*[i] mutant strains, the tubulin signal of the entire outer segment was lower than wild type, but the signal in the MO was reduced to a further lower level than that in the TB (Fig. 7, A–C). ET data showed a significantly larger percentage of microtubules spanning across the TB and MO in *kat-60L1*[i] (Fig. 7, D and E), suggesting that microtubules become longer. Furthermore, in comparison to *c01236/BE6*, the TB in *kat-60L1*[i] contained more microtubules (Fig. 7 F), but the microtubule array in the MO still had a similar size (Fig. 7, D and F). This observation suggests that despite the increase in the number, long microtubules could not significantly improve structural integrity of the microtubule array in the MO, demonstrating the necessity of short microtubules in forming the cytoskeleton in the MOs.

The above point was further confirmed by the observations in the tissue-specific knockdown mutants of Patronin. In two *Patronin*[i] strains, tubulin signals in the TB and MO were weaker than those in wild type (Fig. 7, A–C), consistent with the function of Patronin in stabilizing noncentrosomal microtubules. Interestingly, we noted that in *Patronin*[i], tubulin signal in the MO was higher than that in the TB (Fig. 7, A–C), showing that microtubules in the MO were less susceptible to the reduction in the level of Patronin and suggesting the presence of additional stabilizing factors in the MO. Furthermore, the stronger tubulin signal in the MO in *Patronin*[i] was abolished in the double knockdown mutant (*kat-60L1*[i]; *Patronin*[i]; Fig. 7, A–C), confirming that kat-60L1 is required to form the microtubule array in the MO. The remaining tubulin signal in the TB of *kat-60L1*[i] was

further reduced in the double mutant (Fig. 7, A–C), suggesting that kat-60L1 and Patronin work together to promote the growth of microtubules in the TB. Consistent with this idea, overexpression of Patronin led to the formation of microtubule bundles and disrupted the morphology of the outer segment (Fig. 7 G), likely due to over-stabilizing microtubules, which would interfere with the effects of other microtubule-regulating factors, including that of kat-60L1.

Discussion

Microtubule-based cytoskeleton in fly ES cilia

The structural reconstruction reveals that microtubules in the outer segment are highly organized and stable. They form two structurally separate arrays (Fig. 8). In particular, the array in the MO contains mostly short microtubules, which facilitate the structural optimization of the MO and provide anchoring sites to a large number of mechanosensory molecules (e.g., NompC), thereby serving key sensory functions. Furthermore, the microtubule arrays in the TB and MO are differentially regulated, suggesting dedicated patterning and regulatory mechanisms in the outer segment of fly external mechanoreceptors.

Implications for how the cytoskeleton in the outer segment is formed

The present study provides two implications in understanding how the microtubule arrays in fly sensory cilia are formed. First, a large quantity of microtubules is required to form dense arrays in the outer segment. Kat-60L1 and Patronin together amplify the mass of microtubules. In addition, the presence of a small number of microtubules in *c01236/BE6* implies that there is a kat-60L1–independent mechanism (denoted as X1 in Fig. 8) to assemble microtubules. These microtubules may serve as the initial substrates of kat-60L1 to create more templates. Second, the nanoscopic cytoskeleton in the MO determines the number and spatial arrangement of NompC force-sensitive channels that can be accommodated in the MO. Kat-60L1 coordinates the number and length of microtubules to build the cytoskeleton in the MO, which likely facilitates the structural–mechanical design of the MO, for example, providing adequate anchoring sites for NompC or withstanding resting tensions for optimal mechanosensitivity (Sun et al., 2019a). An ensuing issue is how short microtubules in the MO can be stabilized. The lower susceptibility of the MO microtubules to the reduction in the level of Patronin suggests the presence of additional stabilizing mechanisms (denoted as X2 in Fig. 8).

Cellular roles of kat-60L1 in the outer segment

Our results suggest that kat-60L1 has two functions in fly ES cilia. First, kat-60L1 increases the mass of microtubules in the outer segment. This agrees with the proposed function of microtubule-severing enzymes in amplifying the local mass of
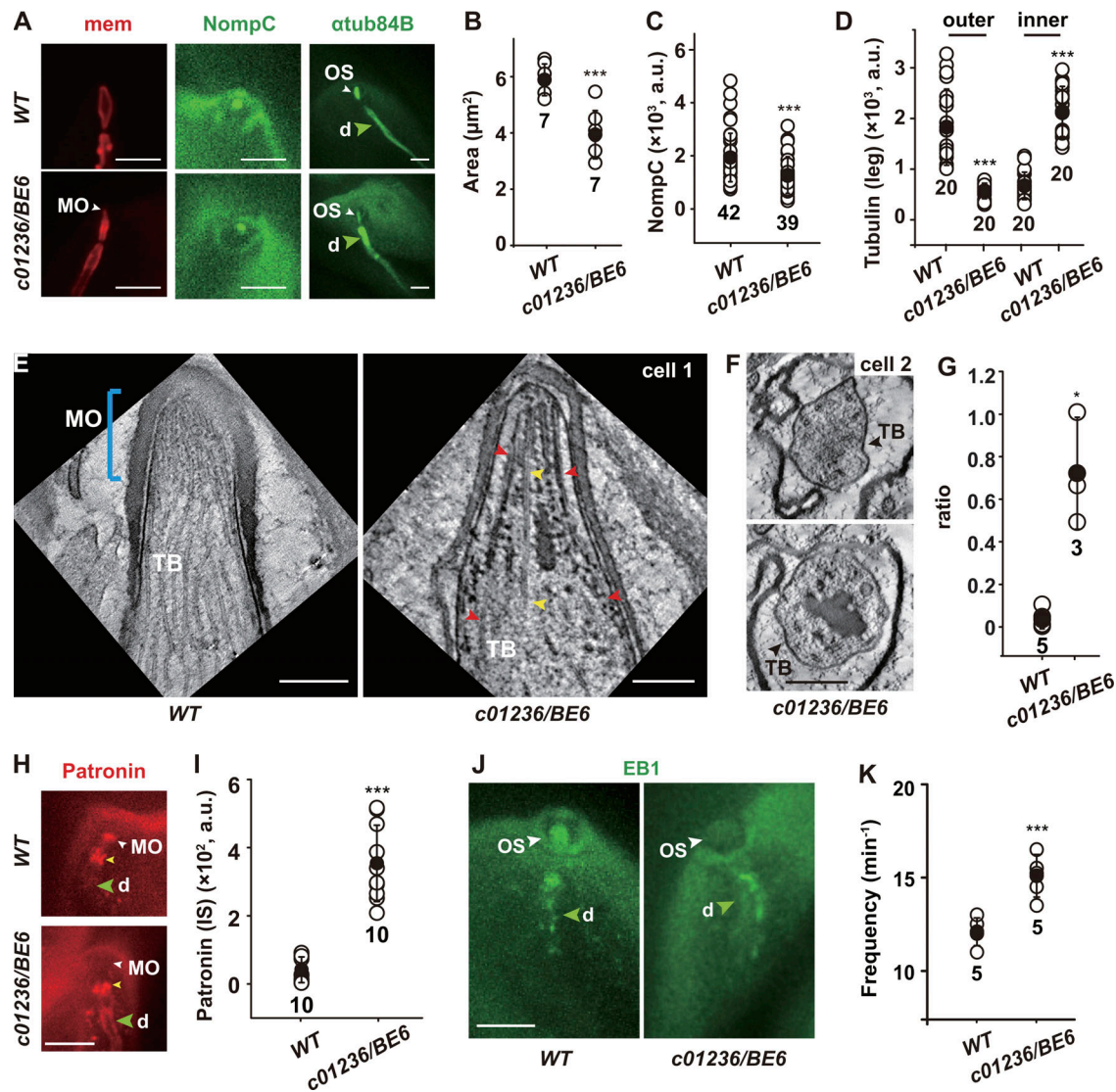
Figure 6. Functions of kat-60L1 in leg receptors. (A) Representative confocal images (lateral view) showing the membrane, NompC, and tubulin labeling of the outer segment. Upper left: *dcx-emap-gal4/uas-cd4-tdTom*. Upper middle: *NompC-gfp-KI*. Upper right: *dcx-emap-gal4/uas-gfp-αtub84B*. Lower left: *dcx-emap-gal4/uas-cd4-tdTom; c01236/BE6*. Lower middle: *NompC-gfp-KI; c01236/BE6*. Lower right: *dcx-emap-gal4/uas-gfp-αtub84B; c01236/BE6*. OS, outer segment; d, dendritic inner segment. Scale bar, 5 μm. **(B–D)** Statistical quantification of the lateral area of the outer segments (B), NompC-GFP signal in the MO (C), and GFP-tubulin signal in the outer and inner segments (D). **(E)** Representative ET slice images (lateral view) of the outer segment in *wild type* (left) and *c01236/BE6* (right). Note that in mutant cells, several microtubules (red arrowheads), including a doublet (yellow arrowheads), spanned across the TB and MO. Scale bars, 0.5 μm. **(F)** Representative ET slice images (cross-sectional view) of the outer segment in *c01236/BE6*. Note that the number of microtubules in the outer segment was largely reduced. Scale bar, 0.5 μm. **(G)** Statistical quantification of the ratio between the number of microtubules that spanned across the TB and MO (see Materials and methods) to the number of MO microtubules. **(H)** Representative confocal images showing Patronin-RFP signals in the leg receptors of *wild type* (*patronin-rfp-KI*) and *c01236/BE6* (*patronin-rfp-KI; c01236/BE6*). White arrowhead, the MO. Yellow arrowhead, the proximal end of the TB. Green arrowhead, dendritic inner segment. Scale bar, 5 μm. **(I)** Statistical quantification of Patronin-RFP signal at the distal region of the inner segment in *wild type* and *c01236/BE6*. **(J)** Representative confocal snapshots of EB1 comets in *wild type* (left, *EB1-tdgfp-KI*) and *c01236/BE6* (right, *EB1-tdgfp-KI; c01236/BE6*). Scale bar, 5 μm. Also see Video 2. **(K)** Statistical quantification of EB1 comet frequency in the inner segment. In B–D, G, I, and K, data are presented as mean ± SD with scattered data points. Two-sided unpaired Student's *t* test was used for statistical analysis. *, P < 0.05; ***, P < 0.001. The number of cells is indicated.

microtubules (McNally and Roll-Mecak, 2018; McNally et al., 2006; Ribbeck and Mitchison, 2006; Roll-Mecak and Vale, 2006; Srayko et al., 2006). Second, kat-60L1 is required to generate short microtubules. It has been shown that microtubule-severing enzymes sculpt cellular microtubule networks; for example, the noncentrosomal microtubule arrays in plant cells (Lindeboom et al., 2013; Zhang et al., 2013) and the meiotic spindle (McNally et al., 2006; Srayko et al., 2006). Previous

studies have also implicated the potential functions of microtubule-severing enzymes in neurons (Sherwood et al., 2004; Stewart et al., 2012; Trotta et al., 2004). However, due to the limited optical resolution, visualizing dense microtubule networks (e.g., in neurons) where the severing activity is potentially important remains challenging (McNally and Roll-Mecak, 2018). ET could be useful in such cases (Srayko et al., 2006). In the present study, our structural reconstruction provides direct evidence to
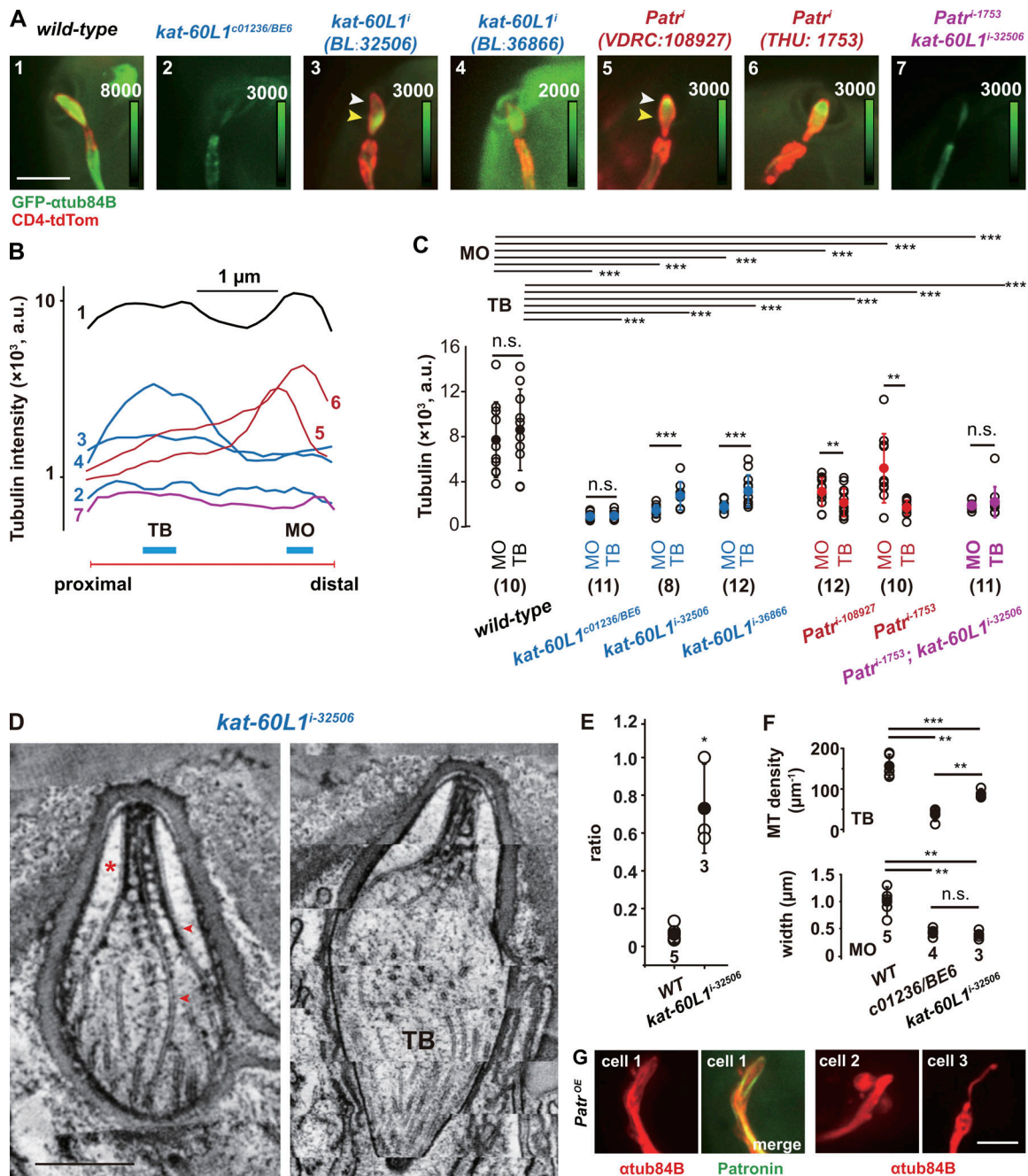
Figure 7. **Nanoscopic cytoskeleton in the MO requires short microtubules. (A)** Representative confocal images (lateral view) showing GFP-tubulin in the outer segment of leg receptors in wild-type and six mutants. 1: +/uas-gfp-αtub84B; dcx-emap-gal4, uas-cd4-tdTom. 2: dcx-emap-gal4/uas-gfp-αtub84B; c01236/BE6. 3: +/uas-gfp-αtub84B; dcx-emap-gal4, uas-cd4-tdTom/kat-60L1^i-32506. 4: uas-gfp-αtub84B/kat-60L1^i-36866; +/dcx-emap-gal4, uas-cd4-tdTom. 5: uas-gfp-αtub84B/patronin^i-108927; +/dcx-emap-gal4, uas-cd4-tdTom. 6: +/uas-gfp-αtub84B; dcx-emap-gal4, uas-cd4-tdTom/patronin^i-1753. 7: dcx-emap-gal4/uas-gfp-αtub84B; patronin^i-1753/kat-60L1^i-32506. Scale bar, 5 µm. **(B)** Representative intensity line profiles of GFP-tubulin signal in the outer segment of leg receptors in wild-type and mutant flies. The numbers correspond to those in A. **(C)** Statistical quantification of GFP-tubulin signal in the TB and MO of leg receptors. The number of flies is indicated in parentheses. Data are presented as mean ± SD with scattered points. For comparison between different genotypes, two-sided unpaired Student's t test was used. For comparison between TB and MO from the same cell, two-sided paired Student's t test was used. **, P < 0.01; ***, P < 0.001. n.s., no significance. **(D)** Representative ET slice images of the outer segment of leg receptors in kat-60L1^i-32506 (two lateral views of the same receptor, but at different layers). Red arrowhead, the long microtubules extending from TB into MO. Red asterisk, the large gap between the microtubule and MO membrane. Note that there were more TB microtubules than in c01236/BE6 (right panel). Scale bar, 0.5 µm. **(E)** Statistical quantification of the ratio between the number of microtubules that spanned across the TB and MO to the number of MO microtubules in the leg receptors in wild type and kat-60L1^i-32506. **(F)** Statistical quantification of microtubule density in the TB (upper) and the width of the microtubule array in the MO (lower) in the leg receptors in wild type, c01236/BE6, and kat-60L1^i-32506. In E and F, the number of cells is indicated. Data are presented as mean ± SD with scattered points. Two-sided unpaired Student's t test. *, P < 0.05; **, P < 0.01; ***, P < 0.001. n.s., no significance. **(G)** Representative confocal images showing the thick microtubule bundles when Patronin was overexpressed (n = 3 cells, dcx-emap-gal4, uas-mcherry-αtub84B/uas-patronin-gfp). Scale bar, 5 µm.
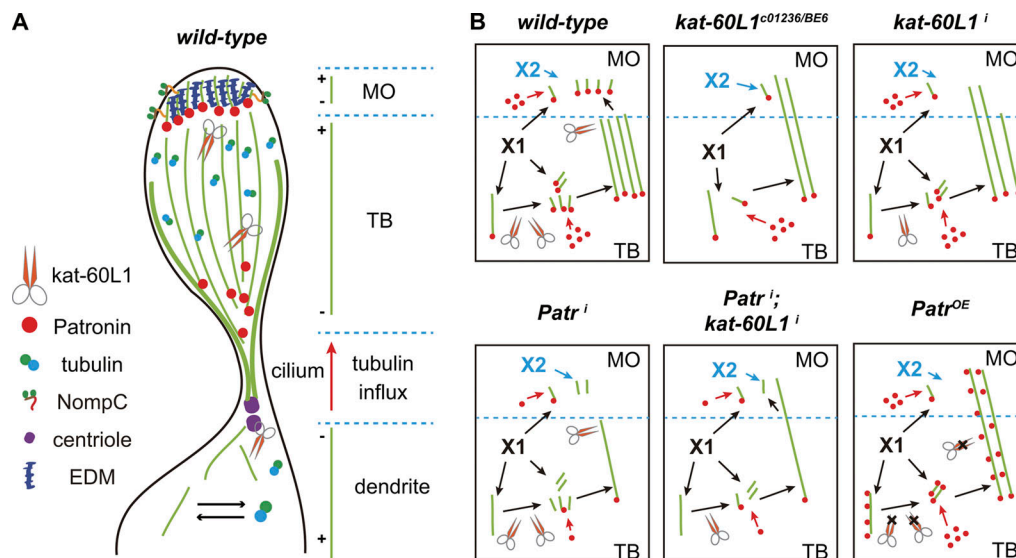
Figure 8. Cartoon schematics. (A) Molecular organization of microtubules in the outer segment. **(B)** Cartoon schematics for all mutants. X1 represents the kat-60L1–independent mechanism that promotes microtubule assembly. X2 represents a stabilizing mechanism for microtubules in the MO. EDM, electron-dense materials.

demonstrate the severing activity of kat-60L1 in fly ciliated sensory neurons, thereby providing new insights into the neuronal and ciliary functions of microtubule-severing enzymes.

A potential caveat to the above conclusion is that the loss of kat-60L1 also changes the homeostatic microtubule dynamics in the inner segment, so it is formally possible that the structural and functional defects in the outer segment might be a secondary effect. However, we do not think this is the case based on three reasons. First, in *kat-60L1*[i], no significant microtubule accumulation was observed in the inner segment (Fig. 7), but the cytoskeleton in the outer segment was also disrupted, suggesting that microtubules in the outer segment are more susceptible to the level of kat-60L1, and that the defects in the outer segment are a primary consequence of losing kat-60L1. Second, more microtubule polymerizations, suggested by the observation of more frequent EB1 comets, are observed in the inner segment in *c01236/BE6* (Fig. 6, J and K), suggesting that the level of free tubulin dimers is fairly normal. Because tubulin is transported or diffuses into cilium as dimers (Craft et al., 2015), we argue that tubulin influx into the cilia, which matters for microtubule dynamics in the outer segment, is not down-regulated in *c01236/BE6*. Third, no major defects in the morphology of dendritic inner segments were observed in *c01236/BE6* (Fig. S4), suggesting that the functional defects can be mostly attributed to the defects in the outer segment.

Kat-60L1: Constructor and destructor

Previous in vitro studies proposed that the cellular effects of microtubule-severing enzymes depend on the ratio between the amount of severing enzymes and the local microtubule dynamics (Kuo et al., 2019; Vemu et al., 2018). Here, we show that in the outer segment, where microtubules are stable and the signal of kat-60L1 is weak, kat-60L1 acts as a constructor, while

in the inner segment, where microtubules are more dynamic and kat-60L1 shows an enriched signal, kat-60-L1 tends to act as a destructor. These results provide an in vivo example that supports the predictions from the previously proposed model (McNally and Roll-Mecak, 2018).

Implication for the functions of katanin family proteins in ciliogenesis

The function of katanin family members has been implicated in ciliogenesis (Dymek et al., 2004; Hu et al., 2014; Sharma et al., 2007), especially in the assembly of central pair microtubules in motile cilia. Fly mechanosensory cilia contain no central pair microtubules (Keil, 1997) but numerous noncentrosomal microtubules. The disruption of the cytoskeleton in the absence of kat-60L1 in fly mechanosensory cilia resembles the loss of central pair microtubules in the katanin mutants of other species. This implies a common component in the assembly mechanism of noncentrosomal microtubules inside cilia, which, however, remains a hypothesis waiting for future studies.

Materials and methods

Flies

All flies were maintained on standard medium at 23–25°C. *w1118* was used as the wild-type strain. *Kat-60L1*[BE6], a null mutant strain, was from Nina Tang Sherwood (Duke University, Durham, NC; Stewart et al., 2012); *Ana1-tdTom*, *B9d1-rfp*, and *Mks1-gfp* strains (endogenously tagged) were provided by Tomer Avidor-Reiss (University of Toledo, Toledo, OH; Basiri et al., 2014). An endogenously tagged *Shot-gfp* strain and *uas-rfp-kat-60L1-long* (Sun et al., 2019b) were from Jose Pastor (Tsinghua University, Beijing, China). *kat-60L1*[i-32506] (BDSC 32506), *kat-60L1*[i-36866] (BDSC 36866), *c01236* (BDSC 10430), *elav-gal4* (BDSC 8765), *uas-gfp-αtub84B* (BDSC 7374), *uas-EB1-gfp* (BDSC 35512),

uasp-gfp-cnn1 (BDSC 7255), *uas-CD4-tdTom* (ch2) (BDSC 35841), *uas-CD4-tdgfp* (BDSC 35836), and *uas-gCamp6s* (BDSC 42746) were from the Bloomington Drosophila Stock Center. *Patronin^{i-108927}* was from the Vienna Drosophila Resource Center (VDRC 108927). *Patronin^{i-1753}* was from the Tsinghua Fly Center (THU 1753). *kat-60L1-gal4*, *kat-60L1-long-gal4*, and *kat-60L1-short-gal4* were generated by cloning the corresponding promoter sequences (Fig. 4 A) into the pptGal4 vector, which were then used to generate the promoter-gal4 strains. To generate the *dcx-emap-gal4* strain, a 1.5-kb upstream sequence in front of the first exon of *dcx-emap* (CG42247) gene was cloned into the pptGal4 vector. To generate the *uas-Patronin-GFP* strain, the cDNA of Patronin was cloned into the pAWG vector (Drosophila Gateway Collection). To generate the *uas-mCherry-αtub84B* strain, the cDNA of αtub84B was cloned into the pMT-mCherry vector, and then the mCherry-αtub84B sequence was subcloned into pHisc-RA-RFP. To generate the *uas-CD4-tdTom* (ch3) strain, the sequence of CD4-tdTom was PCR amplified from strain 35841 (Bloomington Drosophila Stock Center) and cloned into the pUAST-CRT-I-yw2 vector (Xue et al., 2014).

EB1-tdgfp-KI and *patronin-rfp-KI* were generated using the CRISPR/Cas9-based strategy (Ren et al., 2013). The EB1-tdGFP line was generated by directly knocking in tdGFP in the carboxyl terminus of endogenous EB1 with homology-directed repair recombination. The Patronin-RFP line was generated by directly knocking in RFP in the carboxyl terminus of endogenous Patronin with homology-directed repair recombination. Briefly, tdGFP or RFP was first cloned into the pBluescript vector. We used fly genomic DNA as template to amplify the recombination arms, which were then cloned into the donor plasmid. To increase the efficiency, we designed two single-guide RNAs for each gene and cloned them into the U6B-driven vectors. We then injected the injection mix containing the donor plasmid and two single-guide RNA–containing vectors into the embryos of the nos-cas9 strain. G1 and G2 progenies were crossed with the balancer strains. Genomic DNA from individual flies (both G1 and G2) were extracted and screened using PCR. The correct KI lines were further confirmed by DNA sequencing, and lines with no obvious defects were chosen for further experiments.

NompC-gfp-KI was generated by directly knocking in GFP in the carboxyl terminus of endogenous NompC with homology-directed repair recombination (Fig. S1). The gRNA designed to target the NompC gene (gRNA: 5′-GGTGGGCAGACGAGCCATCA-3′) was cloned into the pCFD5 vector as previously described (Port and Bullock, 2016) to get the construct pCFD5-NompC-gRNA. A 1.8-kb sequence upstream of insertion site was ligated with GFP sequences via overlapping PCR. Then, two sequences (2.5 kb and 2.2. kb) corresponding to the 5′ and 3′ sides of the targeting site were inserted flanking the RFP cassette to obtain the final construct pMV-NompC-HR (Xue et al., 2014). To get the GFP KI fly, pCFD5-NompC-gRNA and pMV-NompC-HR were coinjected into the nos-Cas9-attp2 strain as previously described (Ren et al., 2013). Flies with RFP markers were picked as the positive candidates. Finally, six independent lines were confirmed by DNA sequencing.

High-pressure freezing and freeze substitution
High-pressure freezing fixation of fly halteres and legs was developed based on a previous protocol (Sun et al., 2019a). The dissected halteres and legs were submerged in 0.1 M phosphate buffer containing 20% BSA (wt/vol; Sigma-Aldrich; A9647) and 0.05% pluronic acid (wt/vol; Sigma-Aldrich; P2443). The dissected tissue was then sucked into a cellulose capillary tube (Leica; 16706869), which was transferred to a 100-μm-deep membrane carrier (Leica; 16707898) and cryoimmobilized using a Leica EMPACT2/RST or Leica EM HPM100 high-pressure freezer.

Freeze substitution was performed in anhydrous acetone (Electron Microscopy Sciences [EMS]; 10015) containing 1% OsO_4 (EMS; 19110), 0.5% glutaraldehyde (EMS; 16220), 0.1% uranyl acetate (Polysciences; 21447), and 4% pure water with a Leica EMAFS2 automatic freeze substitution device. The samples were kept at –90°C for 40 h, warmed up at a rate of 5°C per hour, incubated at –30°C for 8 h, and warmed up at the rate of 5°C per hour to 0°C. After these steps, the samples were rinsed three times in anhydrous acetone at room temperature and infiltrated with Araldite-epon (EMS; 13940): anhydrous acetone mixtures of 1:3, 1:1, and 3:1 for 1 h at each step, followed by 100% Araldite-epon infiltration overnight. Finally, the samples in fresh Araldite-epon were polymerized at 60°C.

ET
The serial sections (250 nm) were prepared using a Leica Ultracut UCT or Leica EM UC7 microtome and collected on Formvar-coated copper slot grids. For haltere receptors, cross-sections were collected to facilitate data after processing, e.g., microtubule tracing and alignment. For leg receptors, we collected consecutive lateral sections in most cases because the exoskeleton of fly legs often separated from the embedding resin, and the cross-sections, usually with a small tissue area, had a large chance of getting lost or distorted. Post-staining was performed with 2% uranyl acetate in 70% methanol, followed by 0.4% lead citrate (EMS; 17900). 15-nm gold nanoparticles (BBI Solutions; EMGC15) were added to both sides of the sections as the fiducial markers. The dual-axis tilt series ranging from –60° to 60° were acquired using a FEI Tecnai F30 or FEI Tecnai F20 electron microscope (Thermo Fisher Scientific; formerly FEI). An FEI Tecnai F30 electron microscope was equipped with an Axial Gatan US1000 CCD camera and controlled with SerialEM automated acquisition software (Mastronarde, 2005). An FEI Tecnai F20 electron microscope was equipped with a Gatan US4000 (895) CCD camera and controlled with FEI Xplore 3D TEM tomography software.

Serial block-face imaging using focused ion beam (FIB)/scanning electron microscopy
The sample preparation for FIB/scanning electron microscopy was similar to that used for ET except for the embedding medium (Durcupan ACM; Sigma-Aldrich, 44610). For serial FIB milling and scanning electron miscroscopy imaging, a layer of block surface was milled by gallium ion beam, and the block surface was imaged using an electron beam with 2-kV acceleration voltages, 0.4-nA current, and 8-μs dwell time on a FEI Helios NanoLab G3 UC FIB-SEM. After volume data collection, the images were imported into Amira, aligned using the Dual-Beam 3D Wizard module, and exported as a stack of images in

TIF format. The image stacks were then used for structural segmentation.

Structure reconstruction, segmentation, and measurement

The tomography data were processed and analyzed as previously described (Sun et al., 2019a). Tomograms were reconstructed with the IMOD software package (v4.7; Mastronarde, 1997). To stitch the adjacent sections in the z axis, microtubules were traced and used as landmarks. These microtubules were first traced using cylinder correlation and trace correlation lines modules in Amira 6.0 (Thermo Fisher Scientific). The alignment and stitching were performed using the SerialSectionStack module in Amira. The structural segmentation and 3D surface generation for both ET and FIB/scanning electron microscopy data were performed in Amira. All structural measurements in 3D space were performed in Amira.

Spinning-disk confocal imaging and photobleaching

The light microscopy data on living tissue samples were taken using an Andor spinning-disk confocal microscope system equipped with an inverted microscope (Olympus; IX73), an iXon 897 EMCCD, and a 100×UPlanSApo objective (NA 1.40; Olympus) at 25°C. The acquisition software was Andor IQ 3.0. Photobleaching was performed using the Andor Frappa Unit coupled to the spinning disk microscope. The fluorescence recovery (R_{rec}, in percentage) was calculated as

$$R_{rec} = \frac{F_t - F_0}{F_{-1} - F_0} \times 100\%$$

where F_{-1} is the fluorescence signal in the region of interest before bleaching, F_0 is the signal right after bleaching, and F_t is the recovered signal after a period of time (t).

Electrophysiology recording and data analysis

To perform electrophysiology recording of the haltere campaniform receptors, a decapitated adult fly (2–3 d old) was immobilized by wax on a glass slide mounted on a ball-and-socket stage (Newport; M-RN-86). A tungsten electrode was placed near the haltere nerve. The reference electrode was inserted in the thorax. A sharp probe was mounted onto a piezo stack actuator (Physikinstrumente; P216.90), which was driven by a piezo amplifier/controller (Physikinstrumente; E-481 PICA Piezo High-Power Amplifier/Controller,) to apply the mechanical stimuli to the campaniform receptor array in the pedicel of the haltere. We applied a square wave stimulation at 100 Hz. The voltage difference between the reference and recording electrodes was amplified with a differential amplifier (WPI; DAM50 Bio-Amplifier). Labview was used to program the software to control the stimulation and record the signal. The data were sampled at 10 kHz and stored on a computer. Offline data analysis was performed with MATLAB.

Force-induced calcium response in leg receptors

An adult fly (2–3 d old) that expressed GCaMP6s (Ca^{2+} indicator) was immobilized on a 35-mm dish, and its legs were kept stretched using a transparent tape. A glass probe with a spherical tip (60 µm in diameter) was mounted on a piezo actuator (SuZhou Micro Automation Technology Co., Ltd.; PZT 150/7/60 VS12) and was used to apply compressive force (20-µm step) onto the outer segment of leg receptors. The force-induced change in the calcium signal in the soma of leg receptors was then recorded using a spinning-disk confocal microscope equipped with a 100×UPlanSApo objective (NA 1.40; Olympus). The amplitude of the calcium signal was quantified to measure the force-induced responses.

Molecular biology

Total fly RNA was extracted with the RNeasy Kit (Qiagen). The cDNA was synthesized using SuperScript III Reverse Transcription (Thermo Fisher Scientific). All PCRs were performed with Phusion DNA polymerase (New England Biolabs).

Flight test

Flight tests were performed as previously described (Bechstedt et al., 2010). Adult flies (2–3 d) were examined for wing defects and then allowed to recover from carbon dioxide overnight. Standard cylinders coated with paraffin oil were used. Fly vials were turned upside down in a funnel through which flies can fly into the cylinder. When they hit the wall of the cylinder, the flies would get stuck on the wall. The position of each fly was recorded and used for statistical analysis.

Tubulin purification and microtubule polymerization

Porcine tubulin was purified from brain homogenates by cycles of polymerization/depolymerization followed by purification on the tumor overexpressed gene affinity column and with a final subsequent cycle of polymerization/depolymerization (Gell et al., 2011; Widlund et al., 2012). Labeling of tubulin with tetramethylrhodamine (TAMRA) was performed as previously described (Gell et al., 2010, 2011). To prepare taxol-stabilized microtubules, 40 µM tubulin (10% TAMRA labeling) in BRB80 containing 1 mM GTP, 4 mM $MgCl_2$, and 4% DMSO was first incubated on ice for 5 min and then polymerized at 37°C for 30 min. Then, 400 µl of warm BRB80 buffer containing 20 µM taxol was added to stop the reaction and stabilize the microtubules. The taxol-stabilized microtubules were then collected in BRB80 with 20 µM taxol using an Airfuge (Beckman). The stabilized microtubules were subjected to microscope analysis and microtubule spin-down analysis to examine the function of purified kat-60L1.

Microtubule spin-down assay

The spin-down assay was performed as previously described (Varga et al., 2006). Briefly, taxol-stabilized microtubules were diluted in BRB80 supplemented with 20 µM taxol and 0.001% Tween-20 to 0.5 µM tubulin dimer concentration and incubated with 300 nM kat-60L1 (in the presence of 1 mM ATP or ADP) for 30 min at room temperature. Finally, the samples were pelleted using an Airfuge (Beckman). The supernatant and pellet were then analyzed by SDS-PAGE.

Microtubule-severing assay

The in vitro microtubule assay was performed as previously described (Gell et al., 2010). Briefly, taxol-stabilized microtubules were

immobilized on the surface of a silanized coverslip using an anti-TAMRA antibody (Thermo Fisher Scientific; A6397). 300 nM kat-60L1 was added into the reaction in the presence of 1 mM ATP or ADP. The imaging buffer was BRB80 supplemented with 80 mM D-glucose, 0.4 mg/ml glucose oxidase, 0.2 mg/ml catalase, 0.8 mg/ml casein, 1% β-mercaptoethanol, and 0.001% Tween-20. TIRF imaging was performed at 35°C using an Olympus Cell TIRF system with an Andor 897 Ultra EMCCD and a 100×/1.45 NA TIRF objective.

Purification of maltose-binding protein (MBP)–GFP-kat-60L1

The coding region of the kat-60L1-long was modified by addition of an MBP tag followed by a GFP tag on the amino terminus. Then, kat-60L1-long was expressed in *Spodoptera frugiperda* cells using a modified Bac-to-Bac system (Invitrogen). The MBPTrap column (GE Healthcare) was used to purify the recombinant protein according to the manufacturer's instructions. Briefly, the cells were lysed with the lysis buffer (80 mM Pipes, 1 mM EGTA, 1 mM MgCl$_2$, 100 mM KOH, 100 mM KCl, 1 mM DTT, 0.1% Tween-20, and 0.1 mM ATP, pH 6.9). The lysate was first clarified by centrifuging at 80,000 rpm for 15 min. The supernatant was filtered through a 0.22-μm syringe filter and then applied to the MBPTrap column. The column was washed with the lysis buffer. Then the column was equilibrated back to the lysis buffer, and the protein was eluted with 10 mM maltose in lysis buffer. Finally, the protein was subjected to buffer exchange to remove maltose (80 mM Pipes, 1 mM EGTA, 1 mM MgCl$_2$, 100 mM KOH, 100 mM KCl, and 0.1 mM ATP, pH 6.9) and used immediately after the purification (without freezing) to avoid protein aggregation. The purified proteins were analyzed using SDS-PAGE (Coomassie blue staining).

Conventional data plotting and statistical analysis

Data plotting and statistical analysis were performed using Igor Pro 6.11 (WaveMetrics). Box plots (Fig. 4 E and Fig. 5 I) were shown with minimum, lower quartile, median (line in the box), mean (circle), upper quartile, and maximum.

Image analysis
Positioning microtubule ends

The position of individual microtubule ends was determined by inspecting ET volume data using Amira 6.0 (Thermo Fisher Scientific; Fig. S2). For leg receptors, the distalmost tip was set as the reference point. The distance between each microtubule end and the reference point was measured to locate the end. When positioning a microtubule end, we also recorded whether it was the proximal end or the distal end of a microtubule (Fig. 2 E).

Fluorescence signal measurements

To measure the local fluorescent signal of a protein (e.g., GFP-tubulin, NompC-GFP, or Patronin-RFP), the regions of interest were first selected. The shape (e.g., area) and fluorescence intensity of the selected regions were then measured using ImageJ.

Microtubule density

To measure the density of microtubules in volume data, the area of regions of interest was first measured, and then the number of microtubules inside this area (e.g., TB) was counted using

Amira 6.0 (Thermo Fisher Scientific). The density was calculated as the number of microtubules divided by the area.

Width of the cytoskeleton in MO

The width of the cytoskeleton in MO was measured at 500 nm away from the distalmost tip (i.e., the reference point) in the ET reconstructed tomograms using Amira 6.0 (Thermo Fisher Scientific).

The ratio between the number of microtubules that span across the TB and MO to the number of MO microtubules

The number of MO microtubules was directly counted in ET volume data (Fig. 2 E, Fig. 6 E, and Fig. 7 D). Based on our analyses on wild-type cells, MO microtubules in leg receptors were rarely longer than 800 nm, so the MO microtubules whose proximal end was farther than 800 nm away from the distalmost tip (i.e., the reference point) were marked as one spanning across TB and MO. The number of such microtubules was divided by the total number of MO microtubules to get the ratio (Fig. 2 F, Fig. 6 G, and Fig. 7 E).

Online supplemental material

Fig. S1 shows the cartoon schematics of two KI strains and live-cell imaging of fly leg campaniform mechanoreceptors. Fig. S2 shows the representative images that were used to map microtubule ends in the outer segment and to measure microtubule density in the inner segment. Fig. S3 shows the expression pattern, subcellular localization, and severing activity of kat-60L1. Fig. S4 shows the data on the ciliary and dendritic structures in haltere and leg receptors. Fig. S5 shows the ultrastructure of the sensory cilium in the haltere pedicellar campaniform mechanoreceptor in *c01236/BE6*. Video 1 shows the stitched ET volume data and the segmented microtubule model of the outer segment in a wild-type haltere pedicellar campaniform mechanoreceptor. Video 2 shows EB1 comets in the dendritic inner and outer segments of wild-type and mutant leg campaniform mechanoreceptors. Video 3 shows the segmented models of the dendritic outer segments in wild-type and mutant receptors.

References

Basiri, M.L., A. Ha, A. Chadha, N.M. Clark, A. Polyanovsky, B. Cook, and T. Avidor-Reiss. 2014. A migrating ciliary gate compartmentalizes the site of axoneme assembly in Drosophila spermatids. *Curr. Biol.* 24: 2622–2631. https://doi.org/10.1016/j.cub.2014.09.047

Bechstedt, S. 2006. Mechanotransduction in *Drosophila melanogaster*. PhD thesis. Max Planck Institute of Molecular Cell Biology and Genetics, Dresden, Germany. 154 pp.

Bechstedt, S., J.T. Albert, D.P. Kreil, T. Müller-Reichert, M.C. Göpfert, and J. Howard. 2010. A doublecortin containing microtubule-associated protein is implicated in mechanotransduction in Drosophila sensory cilia. *Nat. Commun.* 1:11. https://doi.org/10.1038/ncomms1007

Corey, D.P., and A.J. Hudspeth. 1983. Kinetics of the receptor current in bullfrog saccular hair cells. *J. Neurosci.* 3:962–976. https://doi.org/10.1523/JNEUROSCI.03-05-00962.1983

Craft, J.M., J.A. Harris, S. Hyman, P. Kner, and K.F. Lechtreck. 2015. Tubulin transport by IFT is upregulated during ciliary growth by a cilium-autonomous mechanism. *J. Cell Biol.* 208:223–237. https://doi.org/10.1083/jcb.201409036

Cueva, J.G., A. Mulholland, and M.B. Goodman. 2007. Nanoscale organization of the MEC-4 DEG/ENaC sensory mechanotransduction channel in Caenorhabditis elegans touch receptor neurons. *J. Neurosci.* 27: 14089–14098. https://doi.org/10.1523/JNEUROSCI.4179-07.2007

Dymek, E.E., P.A. Lefebvre, and E.F. Smith. 2004. PF15p is the chlamydomonas homologue of the Katanin p80 subunit and is required for assembly of flagellar central microtubules. *Eukaryot. Cell.* 3:870–879. https://doi.org/10.1128/EC.3.4.870-879.2004

Gell, C., V. Bormuth, G.J. Brouhard, D.N. Cohen, S. Diez, C.T. Friel, J. Helenius, B. Nitzsche, H. Petzold, J. Ribbe, et al. 2010. Microtubule Dynamics Reconstituted In Vitro and Imaged by Single-Molecule Fluorescence Microscopy. *Methods Cell Biol.* 95:221–245.

Gell, C., C.T. Friel, B. Borgonovo, D.N. Drechsel, A.A. Hyman, and J. Howard. 2011. Purification of tubulin from porcine brain. *Methods Mol. Biol.* 777: 15–28. https://doi.org/10.1007/978-1-61779-252-6_2

Gillespie, P.G., and U. Müller. 2009. Mechanotransduction by hair cells: models, molecules, and mechanisms. *Cell.* 139:33–44. https://doi.org/10.1016/j.cell.2009.09.010

Gillespie, P.G., and R.G. Walker. 2001. Molecular basis of mechanosensory transduction. *Nature.* 413:194–202. https://doi.org/10.1038/35093011

Goodwin, S.S., and R.D. Vale. 2010. Patronin regulates the microtubule network by protecting microtubule minus ends. *Cell.* 143:263–274. https://doi.org/10.1016/j.cell.2010.09.022

Hendershott, M.C., and R.D. Vale. 2014. Regulation of microtubule minus-end dynamics by CAMSAPs and Patronin. *Proc. Natl. Acad. Sci. USA.* 111: 5860–5865. https://doi.org/10.1073/pnas.1404133111

Howard, J. 2001. Mechanics of Motor Proteins and the Cytoskeleton. Sinauer Associates, Publishers. Sunderland, MA.

Hu, W.F., O. Pomp, T. Ben-Omran, A. Kodani, K. Henke, G.H. Mochida, T.W. Yu, M.B. Woodworth, C. Bonnard, G.S. Raj, et al. 2014. Katanin p80 regulates human cortical development by limiting centriole and cilia number. *Neuron.* 84:1240–1257. https://doi.org/10.1016/j.neuron.2014.12.017

Keil, T.A. 1997. Functional morphology of insect mechanoreceptors. *Microsc. Res. Tech.* 39:506–531. https://doi.org/10.1002/(SICI)1097-0029(19971215)39:6<506::AID-JEMT5>3.0.CO;2-B

Kuo, Y.W., O. Trottier, M. Mahamdeh, and J. Howard. 2019. Spastin is a dual-function enzyme that severs microtubules and promotes their regrowth to increase the number and mass of microtubules. *Proc. Natl. Acad. Sci. USA.* 116:5533–5541. https://doi.org/10.1073/pnas.1818824116

Lee, H.H., L.Y. Jan, and Y.N. Jan. 2009. Drosophila IKK-related kinase Ik2 and Katanin p60-like 1 regulate dendrite pruning of sensory neuron during

metamorphosis. *Proc. Natl. Acad. Sci. USA.* 106:6363–6368. https://doi.org/10.1073/pnas.0902051106

Liang, X., J. Madrid, H.S. Saleh, and J. Howard. 2011. NOMPC, a member of the TRP channel family, localizes to the tubular body and distal cilium of Drosophila campaniform and chordotonal receptor cells. *Cytoskeleton (Hoboken).* 68:1–7. https://doi.org/10.1002/cm.20493

Liang, X., J. Madrid, R. Gärtner, J.M. Verbavatz, C. Schiklenk, M. Wilsch-Bräuninger, A. Bogdanova, F. Stenger, A. Voigt, and J. Howard. 2013. A NOMPC-dependent membrane-microtubule connector is a candidate for the gating spring in fly mechanoreceptors. *Curr. Biol.* 23:755–763. https://doi.org/10.1016/j.cub.2013.03.065

Liang, X., J. Madrid, and J. Howard. 2014. The microtubule-based cytoskeleton is a component of a mechanical signaling pathway in fly campaniform receptors. *Biophys. J.* 107:2767–2774. https://doi.org/10.1016/j.bpj.2014.10.052

Liang, X., L. Sun, and Z. Liu. 2017. Mechanosensory Transduction in Drosophila Melanogaster. Springer Singapore. Singapore. https://doi.org/10.1007/978-981-10-6526-2

Lindeboom, J.J., M. Nakamura, A. Hibbel, K. Shundyak, R. Gutierrez, T. Ketelaar, A.M. Emons, B.M. Mulder, V. Kirik, and D.W. Ehrhardt. 2013. A mechanism for reorientation of cortical microtubule arrays driven by microtubule severing. *Science.* 342:1245533. https://doi.org/10.1126/science.1245533

Lumpkin, E.A., K.L. Marshall, and A.M. Nelson. 2010. The cell biology of touch. *J. Cell Biol.* 191:237–248. https://doi.org/10.1083/jcb.201006074

Mastronarde, D.N. 1997. Dual-axis tomography: an approach with alignment methods that preserve resolution. *J. Struct. Biol.* 120:343–352. https://doi.org/10.1006/jsbi.1997.3919

Mastronarde, D.N. 2005. Automated electron microscope tomography using robust prediction of specimen movements. *J. Struct. Biol.* 152:36–51. https://doi.org/10.1016/j.jsb.2005.07.007

McNally, F.J., and A. Roll-Mecak. 2018. Microtubule-severing enzymes: From cellular functions to molecular mechanism. *J. Cell Biol.* 217:4057–4069. https://doi.org/10.1083/jcb.201612104

McNally, F.J., and R.D. Vale. 1993. Identification of katanin, an ATPase that severs and disassembles stable microtubules. *Cell.* 75:419–429. https://doi.org/10.1016/0092-8674(93)90377-3

McNally, K., A. Audhya, K. Oegema, and F.J. McNally. 2006. Katanin controls mitotic and meiotic spindle length. *J. Cell Biol.* 175:881–891. https://doi.org/10.1083/jcb.200608117

Nashchekin, D., A.R. Fernandes, and D. St Johnston. 2016. Patronin/Shot Cortical Foci Assemble the Noncentrosomal Microtubule Array that Specifies the Drosophila Anterior-Posterior Axis. *Dev. Cell.* 38:61–72. https://doi.org/10.1016/j.devcel.2016.06.010

Port, F., and S.L. Bullock. 2016. Augmenting CRISPR applications in Drosophila with tRNA-flanked sgRNAs. *Nat. Methods.* 13:852–854. https://doi.org/10.1038/nmeth.3972

Pringle J., S. William, and J. Gray. 1948. The gyroscopic mechanism of the halteres of Diptera. *Philos. Trans. R. Soc. Lond. B Biol. Sci.* 233:347–384. https://doi.org/10.1098/rstb.1948.0007

Ren, X., J. Sun, B.E. Housden, Y. Hu, C. Roesel, S. Lin, L.P. Liu, Z. Yang, D. Mao, L. Sun, et al. 2013. Optimized gene editing technology for Drosophila melanogaster using germ line-specific Cas9. *Proc. Natl. Acad. Sci. USA.* 110:19012–19017. https://doi.org/10.1073/pnas.1318481110

Ribbeck, K., and T.J. Mitchison. 2006. Meiotic spindle: sculpted by severing. *Curr. Biol.* 16:R923–R925. https://doi.org/10.1016/j.cub.2006.09.048

Roll-Mecak, A., and R.D. Vale. 2006. Making more microtubules by severing: a common theme of noncentrosomal microtubule arrays? *J. Cell Biol.* 175: 849–851. https://doi.org/10.1083/jcb.200611149

Sharma, N., J. Bryant, D. Wloga, R. Donaldson, R.C. Davis, M. Jerka-Dziadosz, and J. Gaertig. 2007. Katanin regulates dynamics of microtubules and biogenesis of motile cilia. *J. Cell Biol.* 178:1065–1079. https://doi.org/10.1083/jcb.200704021

Sherwood, N.T., Q. Sun, M. Xue, B. Zhang, and K. Zinn. 2004. Drosophila spastin regulates synaptic microtubule networks and is required for normal motor function. *PLoS Biol.* 2:e429. https://doi.org/10.1371/journal.pbio.0020429

Srayko, M., E.T. O'toole, A.A. Hyman, and T. Müller-Reichert. 2006. Katanin disrupts the microtubule lattice and increases polymer number in C. elegans meiosis. *Curr. Biol.* 16:1944–1949. https://doi.org/10.1016/j.cub.2006.08.029

Stewart, A., A. Tsubouchi, M.M. Rolls, W.D. Tracey, and N.T. Sherwood. 2012. Katanin p60-like1 promotes microtubule growth and terminal dendrite stability in the larval class IV sensory neurons of Drosophila. *J. Neurosci.* 32:11631–11642. https://doi.org/10.1523/JNEUROSCI.0729-12.2012

Stone, M.C., F. Roegiers, and M.M. Rolls. 2008. Microtubules have opposite orientation in axons and dendrites of Drosophila neurons. *Mol. Biol. Cell.* 19:4122–4129. https://doi.org/10.1091/mbc.e07-10-1079

Sun, L., Y. Gao, J. He, L. Cui, J. Meissner, J.M. Verbavatz, B. Li, X. Feng, and X. Liang. 2019a. Ultrastructural organization of NompC in the mechanoreceptive organelle of *Drosophila* campaniform mechanoreceptors. *Proc. Natl. Acad. Sci. USA.* 116:7343–7352. https://doi.org/10.1073/pnas.1819371116

Sun, T., Y. Song, J. Dai, D. Mao, M. Ma, J.Q. Ni, X. Liang, and J.C. Pastor-Pareja. 2019b. Spectraplakin Shot Maintains Perinuclear Microtubule Organization in Drosophila Polyploid Cells. *Dev. Cell.* 49:731–747.e7.

Trotta, N., G. Orso, M.G. Rossetto, A. Daga, and K. Broadie. 2004. The hereditary spastic paraplegia gene, spastin, regulates microtubule stability to modulate synaptic structure and function. *Curr. Biol.* 14:1135–1147. https://doi.org/10.1016/j.cub.2004.06.058

Varga, V., J. Helenius, K. Tanaka, A.A. Hyman, T.U. Tanaka, and J. Howard. 2006. Yeast kinesin-8 depolymerizes microtubules in a length-dependent manner. *Nat. Cell Biol.* 8:957–962. https://doi.org/10.1038/ncb1462

Vemu, A., E. Szczesna, E.A. Zehr, J.O. Spector, N. Grigorieff, A.M. Deaconescu, and A. Roll-Mecak. 2018. Severing enzymes amplify microtubule arrays through lattice GTP-tubulin incorporation. *Science.* 361: eaau1504. https://doi.org/10.1126/science.aau1504

Wang, Y., M. Rui, Q. Tang, S. Bu, and F. Yu. 2019. Patronin governs minus-end-out orientation of dendritic microtubules to promote dendrite pruning in *Drosophila*. *eLife.* 8:e39964. https://doi.org/10.7554/eLife.39964

Widlund, P.O., M. Podolski, S. Reber, J. Alper, M. Storch, A.A. Hyman, J. Howard, and D.N. Drechsel. 2012. One-step purification of assembly-competent tubulin from diverse eukaryotic sources. *Mol. Biol. Cell.* 23: 4393–4401. https://doi.org/10.1091/mbc.e12-06-0444

Xue, Z., M. Ren, M. Wu, J. Dai, Y.S. Rong, and G. Gao. 2014. Efficient gene knock-out and knock-in with transgenic Cas9 in Drosophila. *G3 (Bethesda).* 4:925–929. https://doi.org/10.1534/g3.114.010496

Zhang, Q., E. Fishel, T. Bertroche, and R. Dixit. 2013. Microtubule severing at crossover sites by katanin generates ordered cortical microtubule arrays in Arabidopsis. *Curr. Biol.* 23:2191–2195. https://doi.org/10.1016/j.cub.2013.09.018

Supplemental material

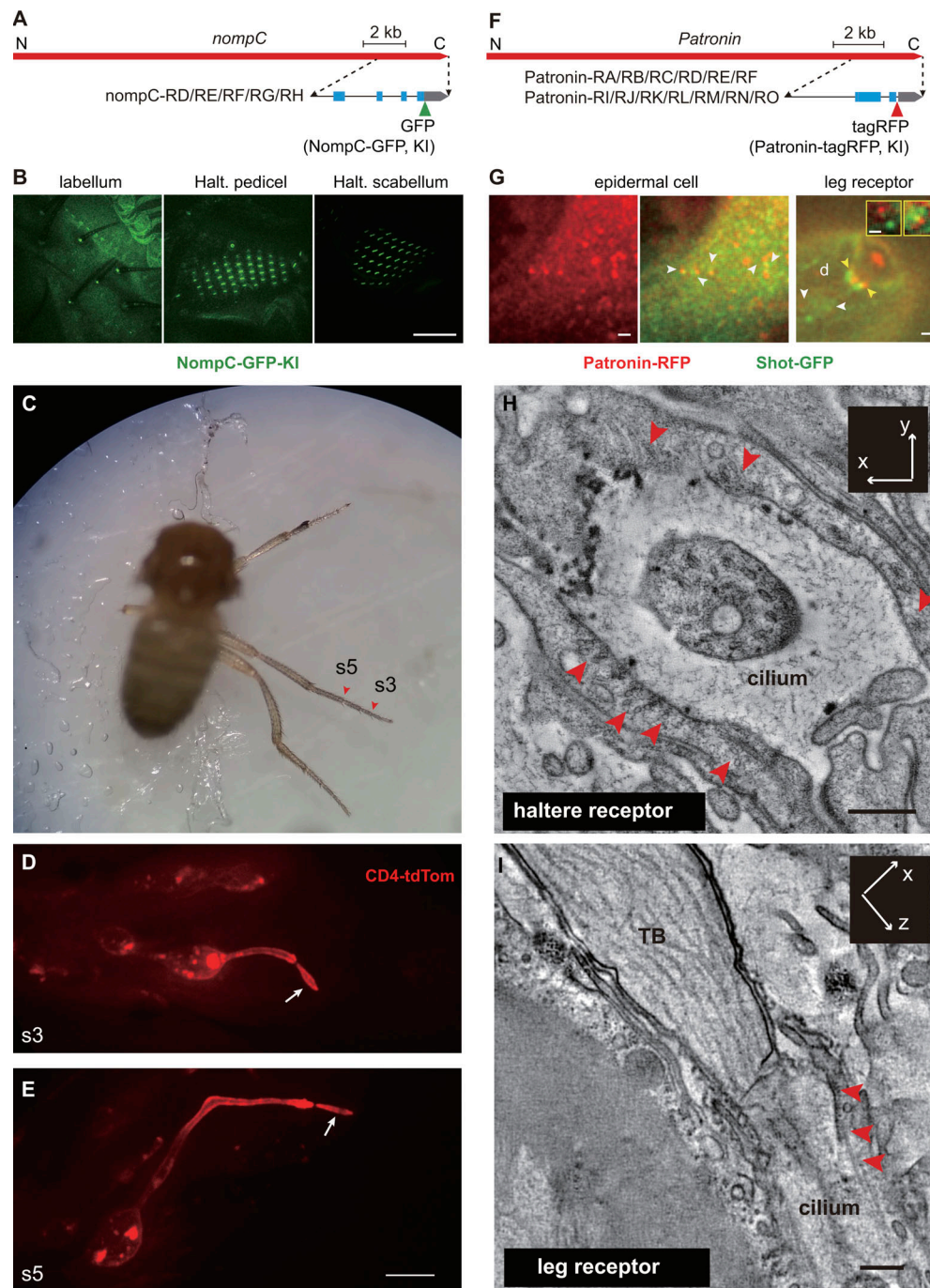Figure S1. **KI strains and live-cell imaging of leg campaniform mechanoreceptors. (A)** Cartoon schematic for the NompC-GFP KI strain (*nompC-gfp-KI*). The insertion site of GFP was indicated. **(B)** Localization of NompC-GFP (*nompC-gfp-KI*) in fly bristle mechanoreceptors (left panel) and haltere campaniform mechanoreceptors (middle and right panels). These observations were consistent with the immunostaining data obtained using a NompC monoclonal antibody (Liang et al., 2011). Scale bar, 20 µm. **(C)** A decapitated fly was kept in a wet chamber, and the locations of leg campaniform mechanoreceptors are indicated (red arrowheads). During imaging, the fly was immobilized on a cover glass using double-sided tape. The three legs on the same body side were covered by the second coverslip to facilitate imaging using an inverted spinning-disk confocal microscope. s3, the third segment. s5, the fifth segment. **(D and E)** Campaniform mechanoreceptors at the third (s3) and fifth (s5) segments of a fly leg (genotype, *dcx-emap-gal4/uas-cd4-tdTom*). The outer segment in these cells is indicated by a white arrow. Scale bar, 5 µm. **(F)** Cartoon schematic for the Patronin-RFP KI strain (*patronin-rfp-KI*). The insertion site of RFP is indicated. Based on the genome annotation in Flybase, all Patronin isoforms were tagged. **(G)** Using an endogenously tagged Shot-GFP (Sun et al., 2019b) as a marker, we showed that Shot-GFP and Patronin-RFP together formed puncta signals in epidermal cells (left and middle panels) and campaniform mechanoreceptors (right panel) in fly legs (genotype, *Shot-GFP/patronin-rfp-KI*). In these puncta, Shot and Patronin showed either contiguous or partially overlapping localizations (white arrowheads, two regions enlarged in the insets, right panel), consistent with the Shot-Patronin foci observed in the fly embryo (Nashchekin et al., 2016). Yellow arrowheads (right) indicate two dot-shaped Shot-Patronin signals that were in the thecogen cell. Scale bars, 1 µm. **(H)** Cross-sectional view (ET slice image) of the cilium and its surrounding structures in a haltere receptor. Scale bar, 250 nm. **(I)** Lateral view (ET slice image) of the structures near the cilium in a leg receptor. Scale bar, 250 nm. In H and I, microtubules in the thecogen cells are indicated by red arrowheads.
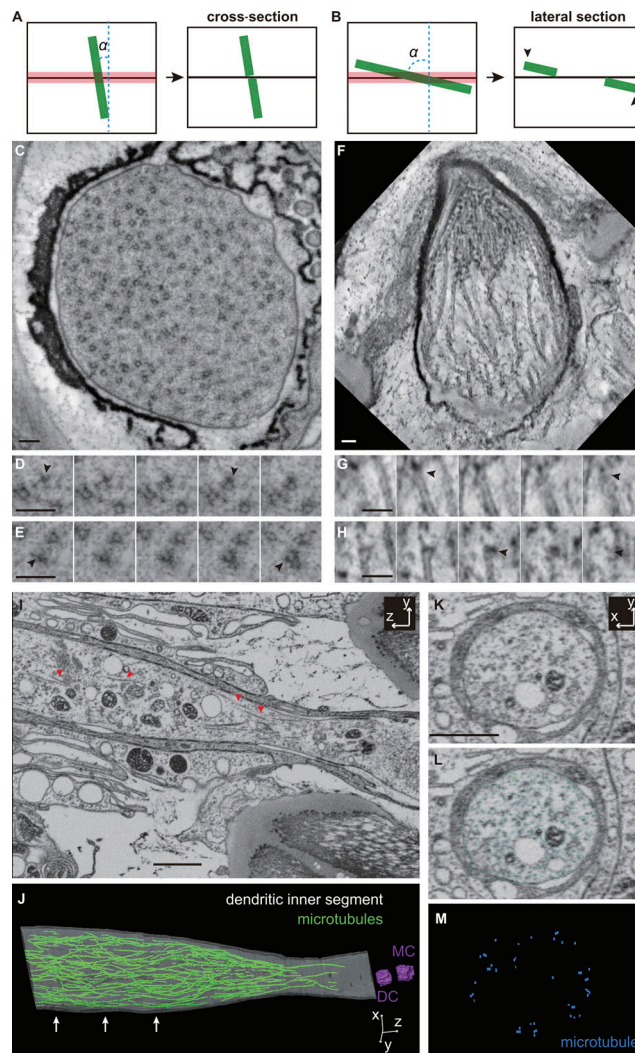
Figure S2.   **Microtubule ends in the outer segment and microtubule density in the inner segment. (A)** Cartoon schematics showing that in cross-sections, microtubules spanning across adjacent sections (along the z axis) can be aligned, and the length can be estimated, because only a short fragment of microtubule might be lost. The red box indicates the region that can be lost during the sample preparations and data processing. We estimated that the loss was ~10–20% in our tomography data. **(B)** Cartoon schematics showing that in lateral sections, microtubules spanning across adjacent sections cannot be well aligned due to the loss of a relatively long fragment in the middle. Therefore, the length of microtubules cannot be well estimated. However, the location of microtubule ends can be determined (black arrowheads). **(C)** A representative cross-sectional view image from the ET volume data of the TB in a haltere campaniform mechanoreceptor. **(D and E)** Two sets of consecutive images (along the z axis) showing microtubule ends appearing within the tissue tomogram (black arrowheads). The adjacent images had a spatial interval of ~4 nm along the z axis (from left to right). **(F)** A representative lateral view image from the ET volume data of the outer segment in a leg campaniform mechanoreceptor. **(G and H)** Two sets of consecutive images showing microtubule ends appearing within the tissue tomogram (black arrowheads). The adjacent images had a spatial interval of ~6 nm. In C–H, scale bars, 100 nm. **(I)** A representative image from the FIB/scanning electron microscopy volume data of a haltere campaniform mechanoreceptor. Red arrowheads indicate the microtubules in the inner segment. Scale bar, 1 μm. **(J)** The segmented model of plasma membrane and microtubules of the inner segment. Two centrioles (MC and DC) were segmented as location markers. White arrows indicate the positions of three cross-sectional images used to quantify the density of microtubules in this cell. One of the three sections and the corresponding segmentation are shown in K–M as an example. **(K)** A representative image showing the cross-sectional view (FIB/scanning electron microscopy slice image) of dendritic inner segment. Scale bar, 1 μm. **(L)** Vesicles and other cellular structures (outlined using blue lines) were manually segmented and excluded in measuring the cross-sectional area of cytoplasmic space. Based on this measurement, we estimated that free cytoplasmic area takes up 51.3 ± 0.04% (n = 3 sections) of the total cytoplasmic area. **(M)** The segmented model of microtubules in the inner segment. Each dot represented one microtubule, and the number of microtubules can be counted. We then estimated the ratio between polymeric and soluble dimeric tubulin in the inner and outer segments as follows. Assuming the density of microtubules is d μm^{-2}, for a 1-μm-long cylinder with a diameter of 1 μm, it contains 0.785d microtubules. Because a 1-μm-long microtubule contains 1,625 tubulin dimers (assuming 13 protofilaments), the total number of tubulin dimers in microtubules is 1,276 d. In the meantime, given that the cytoplasmic concentration of free tubulin dimers is around 10 μM (Howard, 2001), the number of soluble tubulin dimers in this volume is 4,728. Based on our ET data, we counted that the density of microtubules in TB is 156 ± 29 μm^{-2} (n = 5 receptors). If the above cylinder represents a part of TB, it would contain 199,056 polymeric tubulin and 4,728 soluble tubulin dimers. Therefore, polymeric and soluble tubulin dimers take up ~98% and ~2% of the total tubulin signal in the outer segment, respectively. Based on the data in K–M, we counted that the density of microtubules in inner segment is 25 ± 11 μm^{-2} (n = 3 receptors). This predicts that in the inner segment, there are 31,900 polymeric and 4,728 soluble tubulin dimers. Therefore, polymeric and soluble tubulin dimers take up ~87% and ~13% of the total tubulin signal in the inner segment, respectively. DC, daughter centriole; MC, mother centriole.
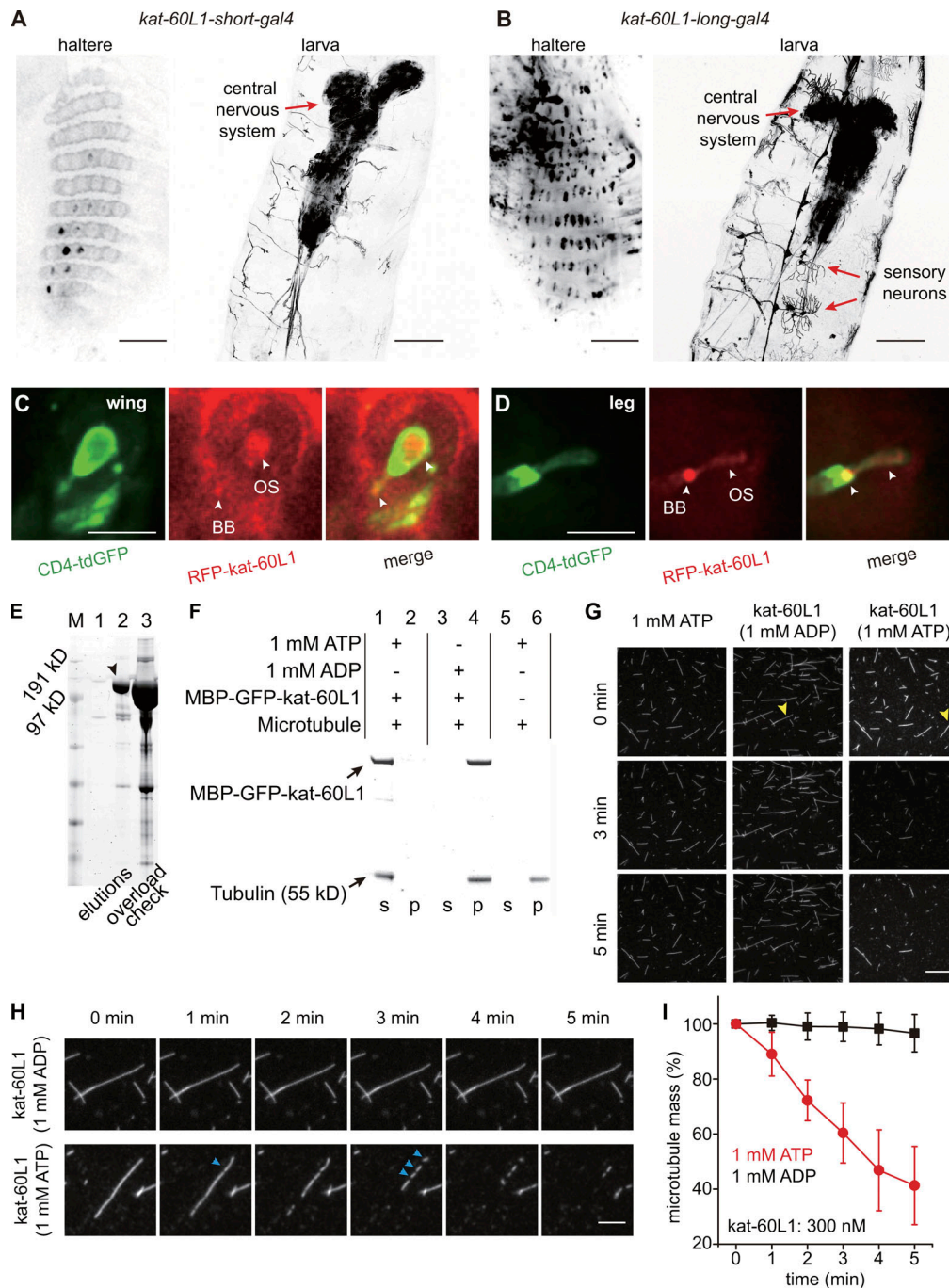
Figure S3. **Expression pattern, localization and severing activity of kat-60L1. (A)** *Kat-60L1-short-gal4* (*kat-60L1-short-gal4; uas-cd4-tdgfp*) drove strong expression in the central nervous system (red arrow, right panel) and weak expression in peripheral sensory neurons (left; confocal images). The expression can only be detected in a few haltere campaniform receptors, and no signal was observed in larval da neurons. Scale bars, 10 µm (left) and 100 µm (right). **(B)** *Kat-60L1-long-gal4* (*kat-60L1-long-gal4; uas-cd4-tdgfp*) drove strong expression in both central nervous system (right panel) and peripheral sensory neurons (left panel and red arrows, right panel; confocal images). Scale bars, 10 µm (left) and 100 µm (right). Note that in A and B, the representative images for haltere and larva are juxtaposed for display. **(C and D)** RFP-Kat-60L1-long showed an enriched signal at the basal body and diffusive signals in the outer segment in wing (C) and leg (D) campaniform mechanoreceptors (confocal images). Genotype, *uas-rfp-kat-60L1-long; kat-60L1-long-gal4/uas-cd4-tdgfp*. Scale bars, 5 µm. **(E)** A protein gel image (Coomassie blue staining) of purified MBP-GFP-kat-60L1 (long isoform, indicated with a black arrowhead). Lane 3 was overloaded to check the protein purity. **(F)** The protein gel image of the microtubule spin-down assay. Kat-60L1 was able to disassemble taxol-stabilized microtubules in vitro in the presence of ATP. In the presence of ADP, kat-60L1 bound to microtubules but could not disassemble them. s, supernatant; p, pellet. **(G)** Representative TIRF images showing that kat-60L1 (300 nM) was able to disassemble taxol-stabilized microtubules in the presence of ATP (1 mM) but not ADP (1 mM). The microtubules indicated with yellow arrowheads are enlarged in H. Scale bar, 10 µm. **(H)** TIRF images showing that kat-60L1 was able to sever microtubules in the presence of ATP (1 mM; lower) but not ADP (1 mM; upper). Scale bar, 5 µm. **(I)** Statistical quantification of the severing activity of kat-60L1 in the presence of ATP (1 mM; *n* = 4 assays) or ADP (1 mM). The total length of microtubules at each time point was measured to reflect the mass of microtubules. Data are presented as mean ± SEM (*n* = 4 assays). BB, basal body. OS, outer segment.
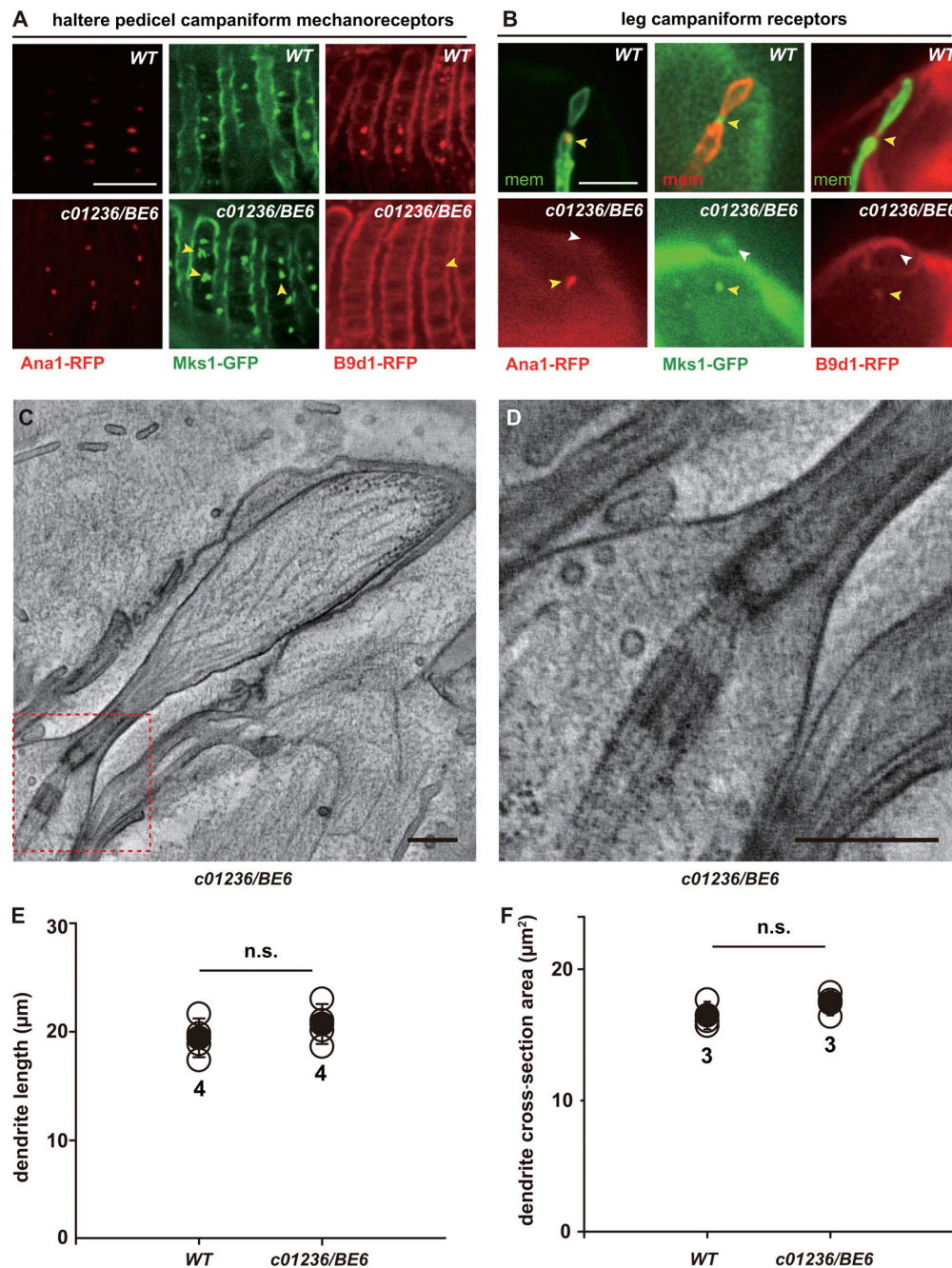
Figure S4. Ciliary structures are disrupted in haltere receptors, but not in leg receptors. (A) Localizations of Ana1-tdTom, Mks1-GFP, and B9d1-RFP (Basiri et al., 2014) in haltere pedicellar campaniform mechanoreceptors in *wild type* (upper) and *c01236/BE6* (lower). Ana1-tdTom (centriole marker) in *c01236/BE6* showed a comparable pattern with wild-type cells, consistent with the presence of two centrioles observed in our ET data. Mks1-GFP (transition zone marker) was present in nearly all mutant receptors, but some of them showed a half-open ring shape, consistent with the enlargement of the cilium in *c01236/BE6*. B9d1-RFP (transition zone marker) was nearly absent in all mutant receptors. These observations confirmed that the ciliary structure was disrupted in the haltere receptors in *c01236/BE6*. Upper left: *Ana1-tdTom*. Upper middle: *Mks1-gfp*. Upper right: *B9d1-rfp*. Lower left: *Ana1-tdTom; c01236/BE6*. Lower middle: *Mks1-gfp; c01236/BE6*. Lower right: *B9d1-rfp; c01236/BE6*. Scale bar, 5 µm. **(B)** Localizations of Ana1-tdTom, Mks1-GFP, and B9d1-RFP in leg receptors in *wild type* (upper) and *c01236/BE6* (lower; $n = 10$ for each genotype). In mutant flies, the external cupola structure (white arrowhead) was used to locate the signal of ciliary markers. The centriole (Ana1-tdTom) and transitional zone (Mks1-GFP and B9d1-RFP) markers appeared to be normal, suggesting that the ciliary structures are intact in mutant leg receptors. Upper left: *dcx-emap-gal4/Ana1-tdTom; +/uas-cd4-tdgfp*. Upper middle: *dcx-emap-gal4/Mks1-gfp; +/uas-cd4-tdTom*. Upper right: *dcx-emap-gal4/B9d1-rfp; +/uas-cd4-tdgfp*. Lower left: *dcx-emap-gal4/Ana1-tdTom; c01236/BE6*. Lower middle: *dcx-emap-gal4/Mks1-gfp; c01236/BE6*. Lower right: *dcx-emap-gal4/B9d1-rfp; c01236/BE6*. Scale bar, 5 µm. **(C and D)** Representative ET slice images of the lateral view of the sensory cilium in a mutant fly (*c01236/BE6*). Note that the ciliary structures (i.e., centriole and cilium) were intact. The region in the dashed box in C was enlarged in D. Scale bars, 500 nm. OS, outer segment. **(E)** Statistical quantification of dendritic length of leg receptors (from confocal images) in *wild type* ($n = 4$ cells) and *c01236/BE6* ($n = 4$ cells). **(F)** Statistical quantification of the cross-section area of dendrite in haltere receptors (from FIB/scanning electron microscopy volume data) in *wild type* ($n = 4$ cells) and *c01236/BE6* ($n = 4$ cells). In E and F, data are presented as mean ± SD with scattered data points. Two-sided unpaired Student's *t* test. n.s., no significance; mem, membrane.
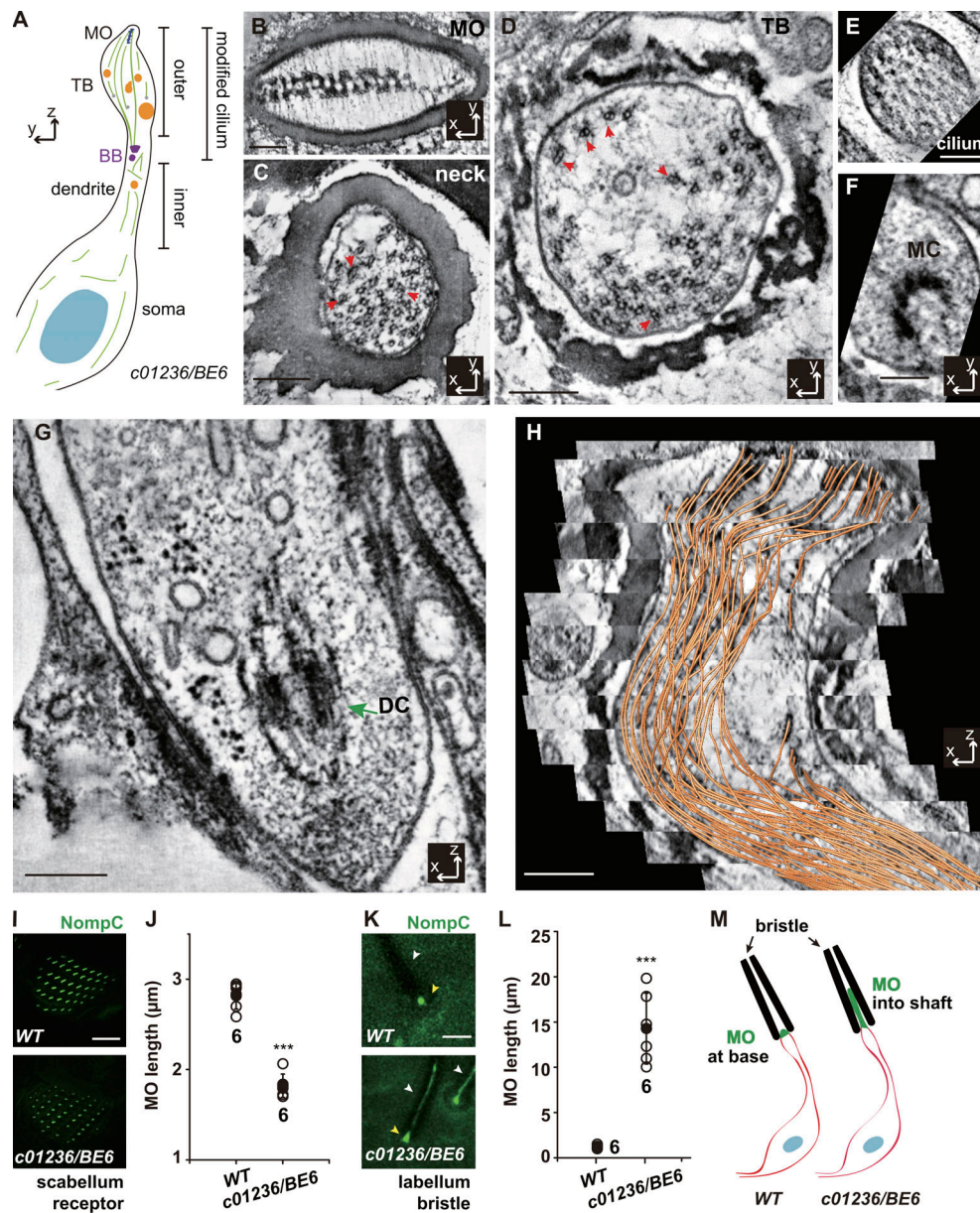
Figure S5. **Structural defects in the haltere pedicellar campaniform mechanoreceptor and other ES mechanoreceptors in *c01236/BE6*. (A)** Cartoon schematic showing the sensory neuron in the haltere pedicellar campaniform mechanoreceptors in *c01236/BE6*. All cellular segments were indicated. In comparison to *wild type* (Fig. 1), the major changes were: (1) the morphology of the outer segment was altered; (2) some vesicles appeared in the outer segment; and (3) microtubules in the outer segment were longer, but the total mass was reduced. **(B–G)** Cross-sectional views (ET slice images) of the MO (B), neck region (C), TB (D), cilium (E), mother centriole (MC; F) and daughter centriole (DC; G) in *c01236/BE6*. Note the appearance of microtubule doublets in the neck and in the central region of the TB (red arrowheads in C and D). **(H)** A representative ET slice image (x-z plane; thickness, ∼1 nm) from the stitched tomographic reconstruction showing that microtubules in the outer segment were long and extended into the MO (orange lines, microtubule traced in the volume data) in *c01236/BE6*. The visualization plane was adjusted to see microtubules. Scale bars in B–H, 250 nm. **(I)** Representative confocal images showing the MO (NompC-GFP labeling) of haltere scabellum receptors. Upper: *nompC-gfp-KI*. Lower: *nompC-gfp-KI; c01236/BE6*. Scale bar, 5 μm. **(J)** Statistical quantification of MO length in haltere scabellum receptors. **(K)** Representative confocal images showing the MO (NompC-GFP labeling) of the bristle receptors in *wild type* and *c01236/BE6*. Upper: *nompC-gfp-KI*. Lower: *nompC-gfp-KI; c01236/BE6*. Scale bar: 5 μm. **(L)** Statistical quantification of MO length in the bristle receptors in *wild type* (n = 6 labela, 30 cells) and *c01236/BE6* (n = 6 labela, 18 cells). **(M)** Cartoon schematics showing the structural change in the MOs of wild-type and mutant bristle receptors. It is intriguing that the mutant MO becomes smaller in campaniform mechanoreceptors but gets longer in bristle receptors. We think that this is because the extracellular structures in these two types of mechanoreceptors are different. In campaniform receptors, the MO develops in a small space surrounded by other extracellular structures. In particular, a dome-like cuticular structure, called a cupola, overlies the distal end of the MO and prevents the MO from elongating further distally (Sun et al., 2019a). In the mutant, because microtubules are longer in length and fewer in number, the cytoskeleton in the MO cannot be well formed, which, in turn, resulted in a poorly developed (i.e., smaller) MO. In bristle cells, there is no cupola-like structure, and the lumen space of the bristle shaft potentially allows the MO (i.e., the NompC-positive region) to further elongate into the bristle lumen (Keil, 1997) when microtubules in the outer segment become much longer in the kat-60L1 mutants. In J and L, data are presented as mean ± SD with scattered data points. Two-sided unpaired Student's *t* test was used for statistical analysis. ***, P < 0.001. The number of halteres or labela is indicated. Six cells were measured for each haltere and three cells for each labelum. BB, basal body.

Video 1. **Stitched ET volume data and the segmented microtubule model of the outer segment in a wild-type haltere pedicellar campaniform mechanoreceptor.** The volume ET data are presented as a stack of images. The microtubules are shown as rods with a diameter of 24 nm. Red, A tubule in doublets. Green, B tubule in doublets. White, microtubules in the outer segment. Yellow, microtubules in the inner segment. Purple, centrioles.

Video 2. **EB1 comets in the dendritic inner and outer segments of wild-type (left) and mutant (right) leg campaniform mechanoreceptors.** The regions of interest, i.e., the inner and outer segments, are indicated. fps, frames per second.

Video 3. **Segmented models of the dendritic outer segments in a *wild-type* receptor (left) and a *c01236/BE6* mutant receptor (right) based on the FIB/scanning electron microscopy volume data.** White (half transparent), membrane. Purple, centriole. Yellow, vesicles. fps, frames per second.